

# Time-lapse Full Waveform Inversion for Subsurface Flow Problems with Intelligent Automatic Differentiation

Dongzhuo Li<sup>1\*</sup>, Kailai Xu<sup>2\*</sup>, Jerry M. Harris<sup>1,2</sup>, Eric Darve<sup>2,3</sup>

<sup>1</sup>Department of Geophysics, Stanford University, Stanford, CA, 94305

<sup>2</sup>Institute for Computational and Mathematical Engineering, Stanford University, Stanford, CA, 94305

<sup>3</sup>Mechanical Engineering, Stanford University, Stanford, CA, 94305

## Key Points:

- We assimilate seismic waveform data to directly invert for intrinsic parameters of subsurface flow (e.g., permeability).
- We adopt an intelligent automatic differentiation strategy with customized operators for high computational efficiency and scalability.

arXiv:1912.07552v1 [physics.geo-ph] 16 Dec 2019

---

\*Both authors contributed equally to this work.

Corresponding author: Dongzhuo Li, [lidongzh@stanford.edu](mailto:lidongzh@stanford.edu)

## Abstract

We describe a novel framework for PDE (partial-differential-equation)-constrained full-waveform inversion (FWI) that estimates parameters of subsurface flow processes, such as rock permeability and porosity, using time-lapse observed data. The forward modeling couples flow physics, rock physics, and wave physics models. For the inverse modeling, we handle the back-propagation of gradients by an intelligent automatic differentiation strategy that offers three levels of user control: (1) At the wave physics level, we adopt the discrete adjoint method in order to use our existing high-performance FWI code; (2) at the rock physics level, we use built-in operators from the `TensorFlow` backend; (3) at the flow physics level, we code customized PDE operators for the potential and nonlinear saturation equations, which highly resemble neural network layers. These three levels of gradient computation strike a good balance between computational efficiency and programming efficiency, and when chained together constitute the coupled inverse system. We use numerical experiments to demonstrate: (1) the three-level coupled inverse problem is superior in terms of accuracy to a traditional strategy; (2) it is able to simultaneously invert for parameters in empirical relationships such as the rock physics models; (3) and, the inverted model can be used for reservoir performance prediction and reservoir management/optimization purposes.

## 1 Introduction

Accurate inversion for the parameters that govern subsurface flow dynamics plays a vital role in addressing energy and environmental problems, such as oil and gas recovery (Teletzke et al., 2010), CO<sub>2</sub> storage (Shi et al., 2013), salt-water intrusion (Beaujean et al., 2014), and groundwater contaminant transport (Reid, 1996; McLaughlin & Townley, 1996). A calibrated flow model can help optimize hydrocarbon production, evaluate environmental risks, and remediate environmental damage.

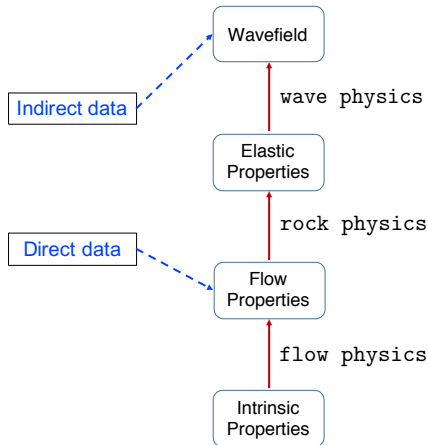


**Figure 1.** The mapping relationship between the physical models that couple flow and seismic properties (data). Note that time-lapse (slow-time) is omitted. Traditionally, intrinsic properties are informed by direct data, i.e., pressure and flow, but can be informed by indirect data, i.e., waves and fields.

There are three types of material properties in this problem: (1) intrinsic rock properties, such as permeability and porosity, related to fluid flow and storage; (2) flow properties such as saturation and pressure; (3) elastic properties such as bulk and shear moduli. Those properties are connected by models of the flow physics, rock

physics, and wave physics as illustrated in Fig. 1. In the aforementioned applications, the inverse problem is to use observed data (e.g., seismic) to estimate intrinsic rock properties, subject to constraints from the physics models. Typically, the observed data can be classified into two types:

1. *Direct* measurements: sparse in-situ flow and pressure data, such as production history and pressure in wells.
2. *Indirect* measurements: seismic, potential fields, and electromagnetic data. In this paper, we consider seismic waveform data.

The seismic data (indirect measurement) are collected through time-lapse surveys, e.g., regular or irregular recordings made months or years apart. To be more specific, fast-time refers to the digital sampling interval of the repeated wavefield recordings, whereas slow-time refers to the evolution time or history of flow in a reservoir. The so-called “fast-time” and “slow-time” are used to emphasize the different time scales for seismic surveys (e.g., days or weeks) and subsurface flow processes (e.g., months or years). In this case, the flow properties are assumed not to change, or change negligibly, in the short period during which the seismic data are recorded, and thus the name seismic snapshots. We also assume that the intrinsic properties such as permeability and porosity do not change with slow-time.

There are inversion challenges with both of the two types of data. On the one hand, traditional methods like history matching use direct measurements or in-situ flow data (e.g., production history and flow pressure in wells) to fit a flow equation for intrinsic properties such as permeability. However, flow data can be only collected from sparsely distributed wells, and the data are usually integrated along the well-bore. Thus, the inversion suffers from large null-space, and the results exhibit reduced resolution.

On the other hand, indirect measurements or soft data such as seismic waves, provide a high volumetric sampling of the reservoir and can reconstruct high-resolution models of elastic properties. However, they do not directly detect the intrinsic properties of interest. Hence, most conventional uses of time-lapse seismic data will first invert for elastic properties that are qualitatively interpreted for the intrinsic rock properties.

Quite a few insightful works have been proposed to incorporate seismic data into flow inversion. The seismic-history matching method (Landa et al., 1997; Huang et al., 1998; Emerick et al., 2007; Volkov et al., 2018) was proposed to treat seismic impedance at each slow-time snapshot as a guide or constraint when fitting the flow equation along from direct data; this approach improves the resolution and well-posedness of the problem. However, there are two shortcomings in this method that we want to improve on. First, for this method the wave physics and flow dynamics are decoupled. Inaccuracies from the intermediate step of seismic impedance inversion yield artifacts in intrinsic properties. Second, the seismic impedance inversion is based on ray theory and simple linear convolution models rather than seismic full-waveform inversion. Recent developments in FWI have provided great improvements in estimates of elastic properties with high spatial resolution and quantitative accuracy (Tarantola, 1984; Virieux & Operto, 2009). Thus, a seismic inversion method fully based on wave equations in line with FWI is highly desirable. Other works have also been proposed to perform coupled-inversion of flow, rock and wave physics. For example, Daley et al. (2011) manually tweaked intrinsic parameters to match seismic data through reservoir simulation, rock physics, and wave propagation simulation. Fohring et al. (2014) constructs a variational inversion scheme that couples seismic traveltime inversion and tracer dynamics (single-phase flow) solved by a specific method (particle in cell method (Evans et al., 1957)), but it is hard to extend this approach to waveform

inversion, and it does not consider other general numerical methods such as (implicit) finite-volume method with upwinding (Aziz, 1979; Crichlow, 1977).

We describe herein an inversion framework that assimilates seismic waveform data to directly and automatically invert for the intrinsic parameters of subsurface flow. This inversion approach couples models for the flow physics, rock physics, and wave physics models. Here we consider a concrete example with the following three key physical components: (1) slow-time subsurface flow model  $\mathcal{S}$ : an immiscible incompressible two-phase flow model that maps permeability to evolution of fluid saturation and pressure; (2) rock physics model  $\mathcal{R}$ : a patchy-saturation model or a Gassmann’s model that maps saturation to rock elastic properties, (3) fast-time seismic wave physics model  $\mathcal{F}$ : elastic wave propagation that maps elastic properties to seismic waveforms recorded at receiver arrays.

Next, we add intelligent automatic differentiation for high computational efficiency and scalability. Our goal is to solve a large-scale partial-differential-equation (PDE) constrained inverse problem with gradient-based optimization methods. However, deriving and implementing the gradients for this coupled system are both nontrivial and laborious. To overcome this difficulty, we propose an automatic differentiation strategy with three levels of complexity. For flow physics models, we use customized PDE operators for one single step in time; for rock physics models, we use built-in operators in an automatic differentiation framework (`TensorFlow` (Abadi et al., 2016)); for the wave physics models, we adopt the discrete adjoint method in order to incorporate an efficient GPU-accelerated FWI code.

In numerical examples, we follow a setup in CO<sub>2</sub> sequestration, in which supercritical CO<sub>2</sub> is injected into a reservoir filled with water. We argue and present evidence that

1. coupled inversion is more accurate than the traditional decoupled inversion, and
2. the inversion can simultaneously invert for empirical closure relationship (e.g., the rock physics model parameters) and intrinsic parameters.

The paper is organized as follows. We first describe the general mathematical formulation of the PDE-constrained inversion problem and coupled physics models. Next, we present the intelligent automatic differentiation method. Finally, we conduct numerical examples, discuss, and offer conclusions.

## 2 Problem Setup

In this section, we first give a general formulation of the time-lapse seismic full-waveform inversion problem for parameters in dynamic geophysical processes. We then discuss in detail the governing equation for the wave propagation and two-phase flow in porous media along with the rock physics that couple flow physics to wave physics.

### 2.1 General Formulation

Mathematically speaking, the problem can be formulated as a PDE-constrained inverse problem. There are two physical processes governed by different PDEs. The first process, the slow-time dynamic flow process, is described by the equation

$$\frac{\partial \mathbf{c}(\mathbf{x}, t)}{\partial t} = \mathcal{S}(\mathbf{c}(\mathbf{x}, t), K(\mathbf{x})), \quad (1)$$

where  $\mathbf{c}$  is the flow property, i.e., fluid saturation,  $K$  is the intrinsic rock property, i.e., permeability. Fluid saturation  $\mathbf{c}$  will affect the elastic properties  $\mathbf{m}$ , e.g., rock bulk

modulus and density through a closure relationship from the rock physics model  $\mathcal{R}$ :

$$\mathbf{m}(\mathbf{x}, t) = \mathcal{R}(\mathbf{c}(\mathbf{x}, t)). \quad (2)$$

The slow-time flow process is monitored indirectly within measurements of duration  $[t_i, t_i + \Delta T_f]$ , where  $t_i$  is the starting slow-time of the  $i$ -th measurement and  $\Delta T_f$  is the fast time interval. Each measurement is a seismic survey conducted by sequentially exciting sources and recording seismic data  $\mathbf{d}_i^{\text{obs}}$  at corresponding receiver positions. We can also compute predictions of wavefield by solving the wave equation

$$\frac{\partial \mathbf{u}_i(\mathbf{x}, t)}{\partial t} = \mathcal{F}(\mathbf{u}_i(\mathbf{x}, t), \mathbf{m}(\mathbf{x}, t)), \quad (3)$$

with  $\mathbf{m}$  as the assumed parameter. Here  $\mathbf{u}$  is the wavefield, which for example can be the field of particle velocity or stress. The time duration of the process Eq. (3) is short compared to Eq. (1), i.e.,  $\Delta T_f \ll T_s$  and therefore we assume that  $\mathbf{m}$  is fixed during  $[t_i, t_i + \Delta T_f]$  and denote  $\mathbf{m}_{t_i}(\mathbf{x}) = \mathbf{m}(\mathbf{x}, t_i)$ . The fast-time scale equation reduces to

$$\frac{\partial \mathbf{u}_i(\mathbf{x}, t)}{\partial t} = \mathcal{F}(\mathbf{u}_i(\mathbf{x}, t), \mathbf{m}_{t_i}(\mathbf{x})) \quad (4)$$

In the same manner of recording observed data, we sample the synthetic wavefield with operator  $\mathcal{Q}$ :  $\mathbf{d}_i = \mathcal{Q}\mathbf{u}_i$ . We can then compute the misfit of synthetic data  $\mathbf{d}$  and observed data  $\mathbf{d}_i^{\text{obs}}$  as  $\mathcal{J}(\mathbf{d}) = \frac{1}{2} \|\mathbf{d}_i^{\text{obs}} - \mathbf{d}_i\|^2$ .

Putting together the above equations with proper boundary and initial conditions  $\mathcal{B}_{\mathcal{F}}$  and  $\mathcal{B}_{\mathcal{S}}$ , we have

$$\min_K J = \sum_{i=1}^{N_s} J_i = \frac{1}{2} \sum_{i=1}^{N_s} \|\mathbf{d}_i^{\text{obs}} - \mathbf{d}_i\|^2 \quad (5)$$

$$\text{s.t. } \mathbf{d}_i(\mathbf{x}, t) = \mathcal{Q}(\mathbf{u}_i(\mathbf{x}, t)) \quad (6)$$

$$\frac{\partial \mathbf{u}_i(\mathbf{x}, t)}{\partial t} = \mathcal{F}(\mathbf{u}_i(\mathbf{x}, t), \mathbf{m}_{t_i}(\mathbf{x})) \quad \mathcal{B}_{\mathcal{F}}(\mathbf{u}_i) = 0 \quad t \in [t_i, t_i + \Delta T_f] \quad (7)$$

$$\mathbf{m}(\mathbf{x}, t) = \mathcal{R}(\mathbf{c}(\mathbf{x}, t)) \quad (8)$$

$$\frac{\partial \mathbf{c}(\mathbf{x}, t)}{\partial t} = \mathcal{S}(\mathbf{c}(\mathbf{x}, t), K(\mathbf{x})) \quad \mathcal{B}_{\mathcal{S}}(\mathbf{c}) = 0 \quad t \in [0, T_s]. \quad (9)$$

The coupled inversion is schematically illustrated in Fig. 2.

## 2.2 Multi-phase Flow in Porous Media

The physics of multi-phase flow in porous media is fundamental to many geoscience fields, such as hydrology, reservoir engineering, glaciology, and volcanology. It underlines the slow-time-scale processes of geophysical time-lapse monitoring problems. As an example, we use the physical model of two-phase immiscible incompressible flow in this paper. This model can describe, at least to the first order, the phenomenon of the displacement of one fluid of the other. Examples include injection of water in a reservoir to produce oil, and injection of supercritical  $\text{CO}_2$  into saline aquifers.

The governing equations are derived from conservation of mass of each phase, and conservation of momentum or Darcy's law for each phase. First, we have

$$\frac{\partial}{\partial t}(\phi S_i \rho_i) + \nabla \cdot (\rho_i \mathbf{v}_i) = \rho_i q_i, \quad i = 1, 2 \quad (10)$$

where Eq. (10) is the mass balance equation, in which  $\phi$  denotes porosity,  $S_i$  denotes the saturation of the  $i$ -th phase,  $\rho_i$  denotes fluid density,  $\mathbf{v}_i$  denotes the volumetric velocity, and  $q_i$  stands for injection or production rates. The saturation of two phases should add up to 1, that is,

$$S_1 + S_2 = 1. \quad (11)$$

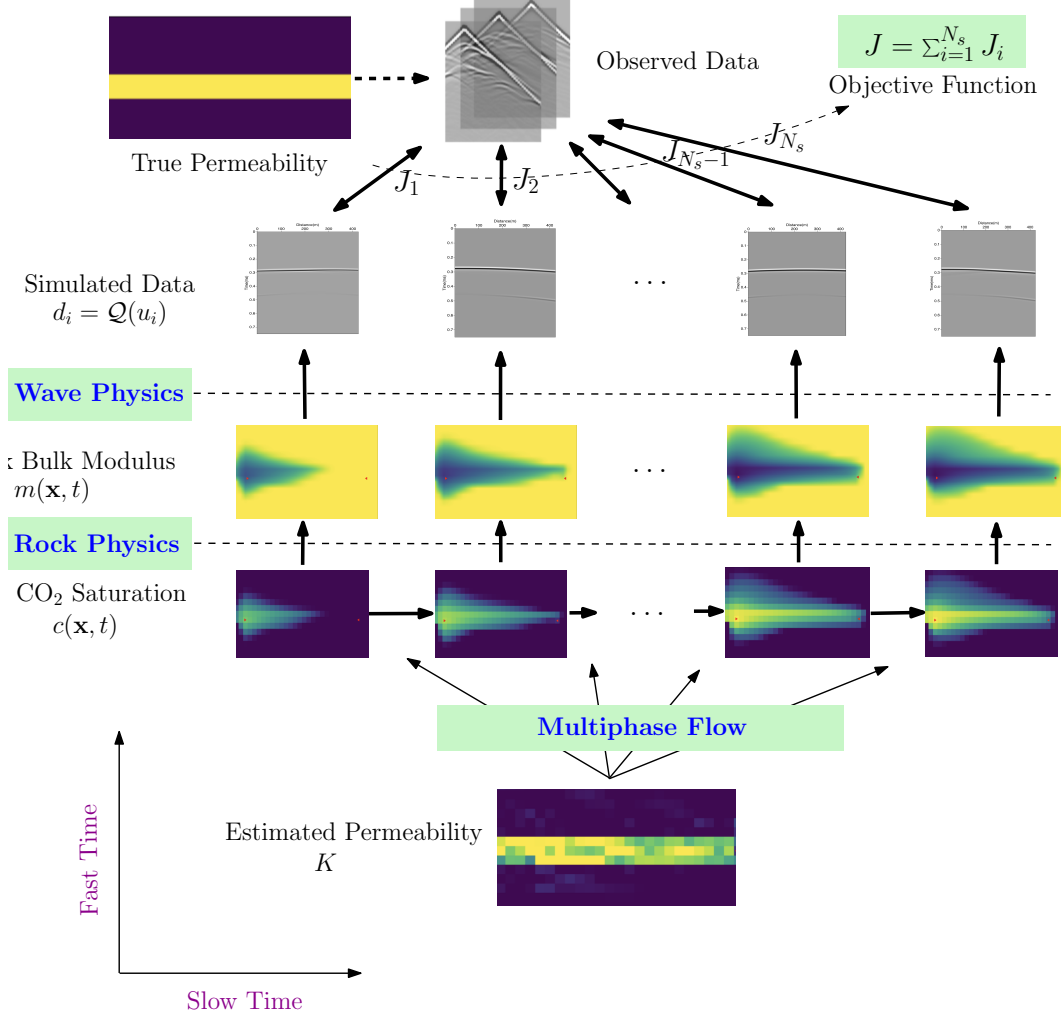


**Figure 2.** Schematic illustration of the coupled inverse problem.

In the remainder of the paper, we inject fluid 2 into the reservoir to replace fluid 1.

Darcy's law yields

$$\mathbf{v}_i = -\frac{K k_{ri}}{\tilde{\mu}_i} (\nabla P_i - g \rho_i \nabla Z), \quad i = 1, 2, \quad (12)$$

where  $K$  is the permeability tensor, which is simplified as a scalar function of space in our model.  $\tilde{\mu}_i$  is the viscosity,  $P_i$  is the fluid pressure,  $g$  is the gravitational acceleration constant, and  $Z$  is the vector in the downward vertical direction. The relative permeability is written as  $k_{ri}$ , which describes how easily one phase flows compared to the other. It is a nonlinear function of saturation of the corresponding phase. Usually, the higher the saturation, the easier the phase is to flow. Empirically, one may use the following equation

$$k_{ri}(S_i) = S_i^a, \quad (13)$$

to describe the relationship, where the power  $a$  is chosen as 2 in our experiments. We define mobilities  $m_i(S_i) = k_{ri}/\rho_i$ ,  $i = 1, 2$ , and the total mobility  $m_t = m_1 + m_2$ . To complete the system, we use another equation to describe the relationship between the two phase-pressures as

$$P_2 = P_1 - P_c(s_2), \quad (14)$$

**Table 1.** Notation for the two-phase flow model.

Symbol	Meaning
$\phi$	porosity
$K$	permeability
$k_{ri}$	relative permeability of fluid $i$
$S_i$	saturation of fluid $i$
$P_i$	pressure of fluid $i$
$P_c$	capillary pressure
$\Psi_i$	potential of fluid $i$
$\Psi_c$	capillary potential
$\mathbf{v}_i$	Darcy's velocity of fluid $i$
$\mathbf{v}_t$	total velocity
$\mathbf{v}_c$	capillary velocity
$\rho_i$	density of fluid $i$
$\tilde{\mu}_i$	viscosity of fluid $i$
$m_i$	mobility of fluid $i$ : $m_i = k_{ri}/\tilde{\mu}_i$
$m_t$	total mobility: $m_t = m_1 + m_2$
$q_i$	injection or production rate of the $i$ fluid
$g$	gravity constant
$Z$	vector of the Z-direction

where  $P_c$  is the capillary pressure, a function of the saturation of the wetting phase  $\alpha$ , but it can be ignored and set to zero in fast-displacement processes.

In a nutshell, the flow physics model maps intrinsic properties to flow properties, for example,

$$K(\mathbf{x}) \longrightarrow S_2(\mathbf{x}, t). \quad (15)$$

We discuss the details of solving the flow equations in Appendix A1.

### 2.3 Rock Physics Models

The second component in the physics system is the rock physics model that links flow properties to elastic properties. All symbols in the rock physics model are listed in Table 2.3. In our example, we construct the relationship between the saturation of the injected fluid  $S_2$  to the rock bulk modulus  $B_r$  and density  $\rho_r$ :

$$B_r, \rho_r = \mathcal{R}(S_2; C_{p1}, C_{s1}, \rho_{r1} B_{f1}, B_{f2}, B_o, \phi, \rho_o, \rho_1, \rho_2), \quad (16)$$

which are also controlled by the other elastic parameters in the parenthesis. Intuitively, the rock bulk modulus and density change with fluid substitution in the rock pore space, as the original and injected fluids may have different bulk moduli and densities. We first use the patchy saturation model that is commonly used for modeling of CO<sub>2</sub> injection processes (Mavko et al., 2009), and then examine a Gassmann's model with Brie's fluid mixing equation (Brie et al., 1995; Mavko et al., 2009). In this model, we ignore the effects of pressure on the elastic properties.

In this paper, we consider two rock physics models: the patchy saturation model and the Gassmann's model with Brie's fluid mixture equations, whose details are presented in Appendix A2.

**Table 2.** Notation for the rock physics models.

Symbol	Meaning
$B_{r1}$	bulk modulus of rock fully saturated with fluid 1
$B_{r2}$	bulk modulus of rock fully saturated with fluid 2
$B_{f1}$	bulk modulus of fluid 1
$B_{f2}$	bulk modulus of fluid 2
$B_o$	bulk modulus of rock grains
$B_{f\_mix}(S_2)$	bulk modulus of fluid mixture
$\mu$	rock shear modulus
$C_{p1}$	P-wave velocity of rock fully saturated with fluid 1
$C_{p2}$	P-wave velocity of rock fully saturated with fluid 2
$C_{s1}$	S-wave velocity of rock fully saturated with fluid 1
$C_{s2}$	S-wave velocity of rock fully saturated with fluid 2
$\phi$	rock porosity
$S_1$	saturation of fluid 1
$S_2$	saturation of fluid 2
$\rho_o$	density of rock grains
$\rho_1$	density of fluid 1
$\rho_2$	density of fluid 2
$\rho_{r1}$	density of rock fully saturated with fluid 1
$\rho_r(S_2)$	density of rock as a function of saturation of fluid 2
$B_r(S_2)$	bulk modulus of rock as a function of saturation of fluid 2

## 2.4 The Elastic Wave Equation

The wave phenomenon can be described by the following velocity-stress formulation of the elastic wave equation:

$$\begin{aligned}
\rho \frac{\partial v_z}{\partial t} &= \frac{\partial \sigma_{zz}}{\partial z} + \frac{\partial \sigma_{xz}}{\partial x} \\
\rho \frac{\partial v_x}{\partial t} &= \frac{\partial \sigma_{xx}}{\partial x} + \frac{\partial \sigma_{xz}}{\partial z} \\
\frac{\partial \sigma_{zz}}{\partial t} &= (\lambda + 2\mu) \frac{\partial v_z}{\partial z} + \lambda \frac{\partial v_x}{\partial x} \\
\frac{\partial \sigma_{xx}}{\partial t} &= (\lambda + 2\mu) \frac{\partial v_x}{\partial x} + \lambda \frac{\partial v_z}{\partial z} \\
\frac{\partial \sigma_{xz}}{\partial t} &= \mu \left( \frac{\partial v_z}{\partial x} + \frac{\partial v_x}{\partial z} \right),
\end{aligned} \tag{17}$$

where  $v_z$  and  $v_x$  are components of the particle velocity vector,  $\sigma_{zz}$ ,  $\sigma_{xx}$ , and  $\sigma_{xz}$  are components of the stress tensor. Density is denoted by  $\rho$  and the Lamé parameters are represented by  $\lambda$  and  $\mu$  (shear modulus). The first Lamé parameter  $\lambda$  and bulk modulus  $B$  that appears in the rock physics model are connected by

$$\lambda = B - \frac{2}{3}\mu. \tag{18}$$

We assume that the depth of the studied area is deep enough so that free surface reflected waves do not appear in the recorded data, and we use convolution perfectly matched layers (CPML) (Martin et al., 2008) on the four boundaries to prevent unrealistic reflected waves.

In summary, the wave physics model maps elastic properties to wavefields:

$$B(\mathbf{x}), \mu(\mathbf{x}), \rho(\mathbf{x}) \longrightarrow \sigma_{zz}(\mathbf{x}, t), \sigma_{xx}(\mathbf{x}, t), \sigma_{xz}(\mathbf{x}, t), v_z(\mathbf{x}, t), v_x(\mathbf{x}, t). \tag{19}$$



### 3 Inversion Method – Intelligent Automatic Differentiation

Automatic differentiation has been successfully used in scientific computing and is one of the major contributors to the success and accessibility of deep-learning technology. Within modern deep-learning frameworks such as TensorFlow (Abadi et al., 2016), there is a suite of built-in differentiable operators (or neural network layers). With those operators, users may construct complex forward mapping functions and automatically obtain gradients. Besides, those frameworks offer high-performance computing options, such as GPU acceleration and graph-based parallelization. Those features are highly desirable when implementing complicated functions such as rock physics models. However, it is computationally inefficient to solve PDEs with these built-in operators or layers. Also, automatic differentiation needs to store intermediate variables for gradient back-propagation, which is also demanding for memory resources.

On the other hand, the so-called adjoint method is widely used for large-scale PDE-constrained inverse problems, such as full-waveform inversion, history matching (Oliver & Chen, 2011; R. Li et al., 2001), 4D variational weather data assimilation (Wang et al., 2001), ocean model inversion (Marotzke et al., 1999), etc. The adjoint method requires analytic derivations of the adjoint equations and gradients. Here we follow the “discretize-then-optimize” philosophy, which means that one first discretizes the forward equations and then makes the following derivations according to the Lagrange multiplier method. We review the details of the discrete adjoint method in Appendix B and illustrate its application to elastic FWI in Appendix D. Once the adjoint equations and formulae of gradients are obtained, one may use various techniques to optimize computation efficiency and reduce the memory footprint. For example, it is not possible to store the whole history of forward wave propagation, so we only store wavefields at the boundaries, and reverse the forward wave equations in time to recompute the forward wavefields. The users can adopt other memory-saving strategies, such as saving a few frequency components (Zhang et al., 2018) or using check-pointing methods (Anderson et al., 2012). It is possible to apply the discrete adjoint method to the whole subsurface flow FWI problem, but the derivations are time-consuming, error-prone, and inflexible, especially when dealing with systems where there are complicated time-stepping schemes and mappings between variables. After all, the derivations are purely mechanical and should be automated.

Therefore, we propose an intelligent automatic differentiation strategy that provides different levels of customization. It combines native automatic differentiation and the discrete adjoint method, such that we can achieve a good balance between computational efficiency and implementation efficiency or flexibility. This is realized by implementing customized PDE operators with gradient computation capabilities that resemble neural network layers in deep-learning frameworks.

As we show in Appendix C, automatic differentiation and discrete adjoint method are equivalent. The only difference is that automatic differentiation requires a specific input-output interface in which we only need to implement two methods for each customized operator:

1. Forward operation  $f_n$ : compute the output by solving a PDE:

$$\mathbf{u}_{n+1} = f_n(\mathbf{u}_n, \theta), \quad (20)$$

where  $\mathbf{u}_n$  is a physical quantity that the PDE describes, such as fluid saturation, pressure in flow equations or wavefield (e.g., particle velocity, stress) in wave equations at time step  $n$ , and  $\theta$  is the parameter of the PDE. The forward-modeling operator  $f_n$  symbolically represents the numerical solving of the PDE at time step  $n$ .

2. Backward operation  $b_n$ : given gradient  $\frac{\partial \mathcal{J}}{\partial \mathbf{u}_{n+1}}$ , compute  $\frac{\partial \mathcal{J}}{\partial \mathbf{u}_{n+1}} \frac{\partial f_n}{\partial \mathbf{u}_n}$  and  $\frac{\partial \mathcal{J}}{\partial \mathbf{u}_{n+1}} \frac{\partial f_n}{\partial \boldsymbol{\theta}}$  with the chain rule. The backward process sprays the gradient of the objective function with respect to the output to the input variables:

$$\frac{\partial \mathcal{J}}{\partial \mathbf{u}_{n+1}} \frac{\partial f_n}{\partial \mathbf{u}_n}, \quad \frac{\partial \mathcal{J}}{\partial \mathbf{u}_{n+1}} \frac{\partial f_n}{\partial \boldsymbol{\theta}} = b_n \left( \frac{\partial \mathcal{J}}{\partial \mathbf{u}_{n+1}}, \mathbf{u}_{n+1}, \mathbf{u}_n, \boldsymbol{\theta} \right). \quad (21)$$

Note that only the matrix-vector product needs to be implemented, and there should be no need to construct Jacobian matrices like  $\frac{\partial f_n}{\partial \mathbf{u}_n}$  explicitly.

The customized PDE operators enable two different levels of customization. For example,

1. the forward process can be wave propagation plus misfit computation, and the backward gradient is computed by the adjoint method. In other words, we encapsulate the entire FWI in an operator.
2. the forward process can be a forward step in the numerical solving of PDEs. This level of customization is helpful when the forward step is numerically complicated. For example, in our flow simulations, we solve nonlinear equations with the Newton-Raphson method and use implicit-time stepping.

To be more specific about the second level of customization, for explicit time-stepping, the implementation of `backward` is straight-forward, as one can usually derive it from the forward code directly. However, we need to employ special tricks for the implicit time-stepping. Now we consider a problem with implicit constraints:

$$\begin{aligned} \min_{\mathbf{u}_1, \boldsymbol{\theta}} f_4(\mathbf{u}_1, \mathbf{u}_2, \mathbf{u}_3, \mathbf{u}_4), \\ \text{s.t. } g_1(\mathbf{u}_2, \mathbf{u}_1, \boldsymbol{\theta}) = 0, \\ g_2(\mathbf{u}_3, \mathbf{u}_2, \boldsymbol{\theta}) = 0, \\ g_3(\mathbf{u}_4, \mathbf{u}_3, \boldsymbol{\theta}) = 0, \end{aligned} \quad (22)$$

where the set of equations  $g_n(\mathbf{u}_{n+1}, \mathbf{u}_n, \boldsymbol{\theta}) = 0$  ( $n = 1, 2, 3$ ) establish the forward mappings  $\mathbf{u}_{n+1} = f_n(\mathbf{u}_n, \boldsymbol{\theta})$ , ( $n = 1, 2, 3$ ), respectively.

However, the programming interface for `backward` is still to compute

$$\frac{\partial \mathcal{J}}{\partial \mathbf{u}_{n+1}} \frac{\partial f_n}{\partial \mathbf{u}_n}, \quad (23)$$

when we are supplied with  $\frac{\partial \mathcal{J}}{\partial \mathbf{u}_{n+1}}$ .

We compute them using the following technique: Take the partial derivative with respect to the interested parameter (e.g.,  $\mathbf{u}_n$ ) on the constraint equation  $g_i(\mathbf{u}_{n+1}, \mathbf{u}_n, \boldsymbol{\theta}) = 0$  and obtain

$$\frac{\partial g_n}{\partial \mathbf{u}_{n+1}} \frac{\partial f_n}{\partial \mathbf{u}_n} + \frac{\partial g_n}{\partial \mathbf{u}_n} = 0, \quad (24)$$

and thus

$$\frac{\partial f_n}{\partial \mathbf{u}_n} = - \left( \frac{\partial g_n}{\partial \mathbf{u}_{n+1}} \right)^{-1} \frac{\partial g_n}{\partial \mathbf{u}_n}. \quad (25)$$

Therefore,

$$\frac{\partial \mathcal{J}}{\partial \mathbf{u}_{n+1}} \frac{\partial f_n}{\partial \mathbf{u}_n} = - \frac{\partial \mathcal{J}}{\partial \mathbf{u}_{n+1}} \left( \frac{\partial g_n}{\partial \mathbf{u}_{n+1}} \right)^{-1} \frac{\partial g_n}{\partial \mathbf{u}_n}. \quad (26)$$

If we let

$$\boldsymbol{\lambda}_{n+1}^T = - \frac{\partial \mathcal{J}}{\partial \mathbf{u}_{n+1}} \left( \frac{\partial g_n}{\partial \mathbf{u}_{n+1}} \right)^{-1}, \quad (27)$$

then we can get  $\lambda_{n+1}$  by solving the following linear system

$$\left(\frac{\partial g_n}{\partial \mathbf{u}_{n+1}}\right)^T \lambda_{n+1} = -\left(\frac{\partial \mathcal{J}}{\partial \mathbf{u}_{n+1}}\right)^T, \quad (28)$$

and then can get

$$\frac{\partial \mathcal{J}}{\partial \mathbf{u}_{n+1}} \frac{\partial f_n}{\partial \mathbf{u}_n} = \lambda_{n+1}^T \frac{\partial g_n}{\partial \mathbf{u}_n}. \quad (29)$$

To summarize, we (1) solve linear system Eq. (28) for adjoint variables  $\lambda_i$ , and (2) compute the matrix-vector product as in Eq. (29).

## 4 Numerical Experiments

### 4.1 Coupled vs. Decoupled Inversion

Our examples are inspired by CO<sub>2</sub> sequestration projects for the reduction of CO<sub>2</sub> emission into the atmosphere. In this example, an injection well injects super-critical CO<sub>2</sub> at a constant rate. It would be more accurate to implement a constant-flow-rate boundary condition to represent an open aquifer, but for simplicity we put another well that produces water displaced by CO<sub>2</sub> as an artificial approximation.

The flow physics can be approximated by immiscible incompressible two-phase flow, even though the model can be much more complicated. As the saturation of CO<sub>2</sub> increases, the bulk modulus and density of the saturated rocks change according to certain rock physics models. These changes in elastic properties can be sensed by elastic waves.

The dimension of the permeability models is  $450 \times 900 \times 10$  m, with 15 cells in the depth direction, 30 cells in the horizontal direction. Each cell is a  $30 \times 30 \times 10$  m block. In the true model, the background permeability is 20 millidarcy (md), while there is a high-permeability layer of 120 md in the middle, as shown in Fig. 3. In the initial model, the permeability in the whole model is 20 md. Before injection, the reservoir was filled with water, whose density is  $1053.0 \text{ kg/m}^3$  and viscosity is 1.0 centipoise (cP). The injected supercritical CO<sub>2</sub> has a density of  $501.9 \text{ kg/m}^3$  and a viscosity of 0.1 cP. The water injection rate was  $0.005 \text{ m}^3/\text{s}$  and the production well produces water at a rate of  $0.005 \text{ m}^3/\text{s}$  as well. We simulated 51 slow-time steps at intervals of 20 days, which gives 1000-day total simulation time. Eleven of the 51, including the initial state, are used for slow-time measurements.

Of course the CO<sub>2</sub> plume favors the highly permeable layer (Fig. 4) and migrate from the injection well (red triangle on the left) to the production well (red triangle on the right), while if CO<sub>2</sub> is injected in a homogeneous reservoir, the plume expands more symmetrically towards the production well with slightly upward movement due to buoyancy.

We up-sampled the saturation evolution maps to a spatial grid interval of 3 m, while keeping the vertical and horizontal dimensions the same. Then, the saturation maps were transformed to elastic properties, Lamé parameter  $\lambda$ ,  $\mu$  and density  $\rho$  in our case, with the patchy saturation rock physics model.

We conducted 11 crosswell seismic surveys to measure the elastic property evolutions with the slow time. In the base case, there were 15 seismic sources and 142 receivers separated by 873 m. The source time function was a Ricker wavelet with a dominant frequency of 50 Hz. The seismic simulation time step was 0.00025 s, and the whole simulation time was 0.75 s. The shot gathers of the 8th source at the first and the eleventh survey are shown in Fig. 6. In each shot gather, the prominent events are a strong P-wave followed by a weaker S-wave. We see a slight delay in arrival time

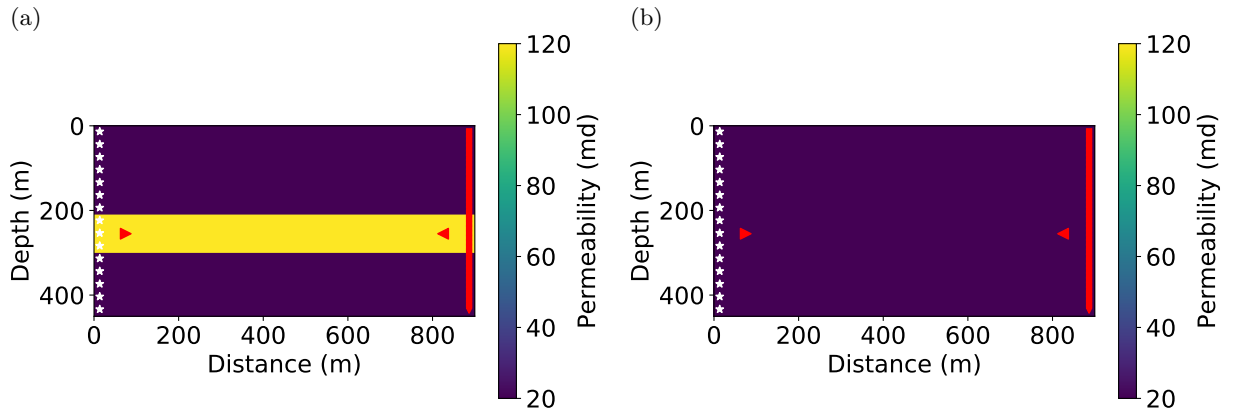


**Figure 3.** True and initial permeability models.

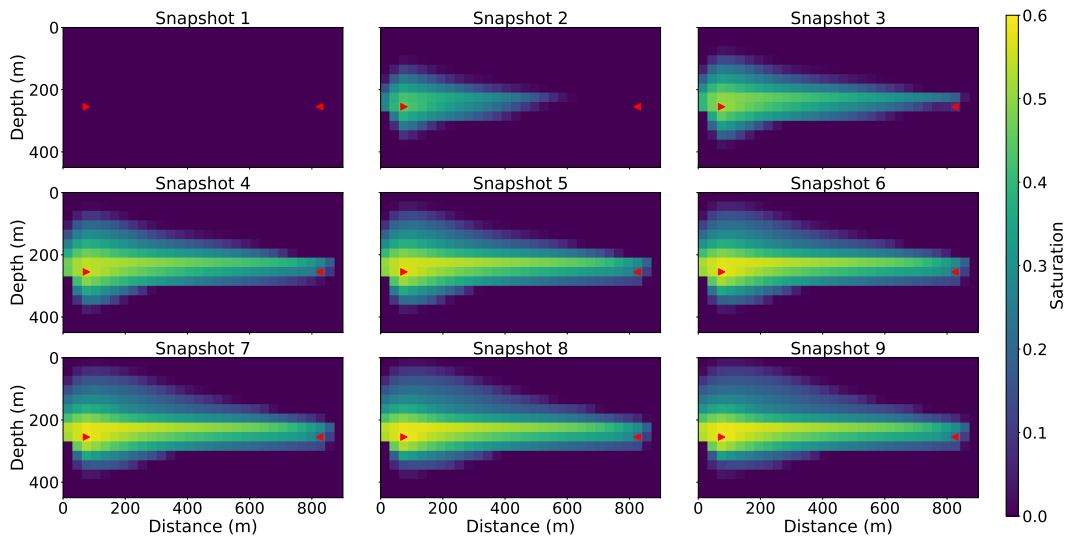


**Figure 4.** Evolution of CO<sub>2</sub> saturation of the first 9 stages with the true permeability model.

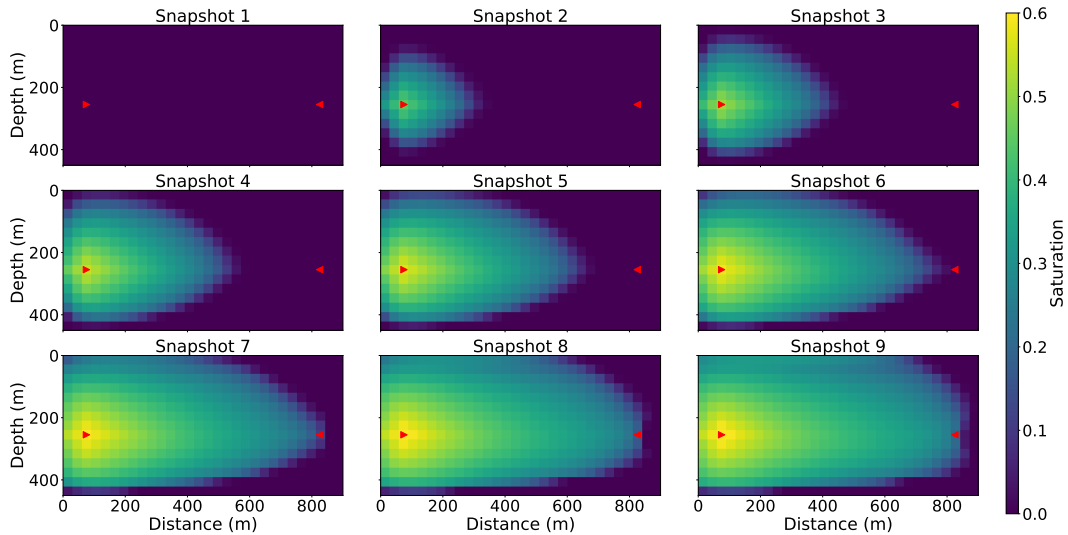


**Figure 5.** Evolution of CO<sub>2</sub> saturation of the first 9 stages with the initial permeability model.

from the 1st to 11th survey, as well as slight changes in amplitude and wavefront shape in the last survey.

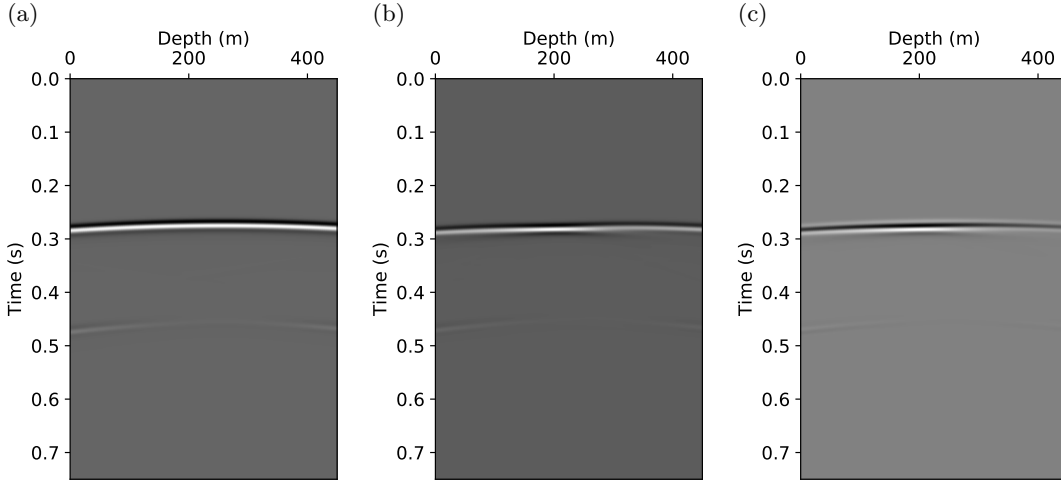


**Figure 6.** Seismic shot gathers of the 8th source. (a) Survey 1, (b) survey 11, (c) difference between (a) and (b).

The optimization problem was solved by the L-BFGS-B method (Byrd et al., 1995) with a box constraint on the permeability value between 10 md and 130 md.

In the coupled inverted model (Fig. 8(a)), the high permeability layer was well constructed, though there are minor fluctuations in the value within the layer. To quantify the inversion accuracy, we define the mean-squared-error (MSE) measure between the true and the inverted permeability models as

$$\text{MSE} = \frac{1}{N_z} \frac{1}{N_x} \sum_{i=1}^{N_z} \sum_{j=1}^{N_x} (K_{ij}^{\text{true}} - K_{ij}^{\text{inv}})^2, \quad (30)$$

where  $N_z$  and  $N_x$  are the two dimensions of discretized permeability models. We found that the MSE of the model from coupled inversion is 218.71.

There exists a traditional choice for permeability field inversion, which we term **decoupled** inversion: one may separately invert for elastic properties at each snapshot using FWI, and then use the inverted elastic properties as data to fit the flow equation to reconstruct the hidden intrinsic parameter field, similar to the seismic history matching methods that we described in the introduction. This strategy is relatively easier to implement but ignores the slow-time dynamics of the coupled inversion process. The inverted results for each survey may have artifacts from various sources. If they are treated as observed data to fit the slow-time process, then we expect that the final inversion result would exhibit stronger artifacts than that from the coupled inversion. We demonstrate this below using the same scenario settings as the base case (11 surveys, all sources). Fig. 7 shows the inverted values for the first Lamé parameter  $\lambda$  from survey 2 to 10. Although we observe that the general shape of CO<sub>2</sub> plume is reconstructed, artifacts due to limited aperture and strong artifacts at source locations exist. We then fitted the flow equation using  $\ell_2$ -norm using the inverted Lamé  $\lambda$  values as the data. To reduce the effects of artifacts at the seismic source and receiver locations, we excluded the left most and right most parts that include the sources and receivers for inversion, and obtained the result shown in Fig. 8(b). Compared to the

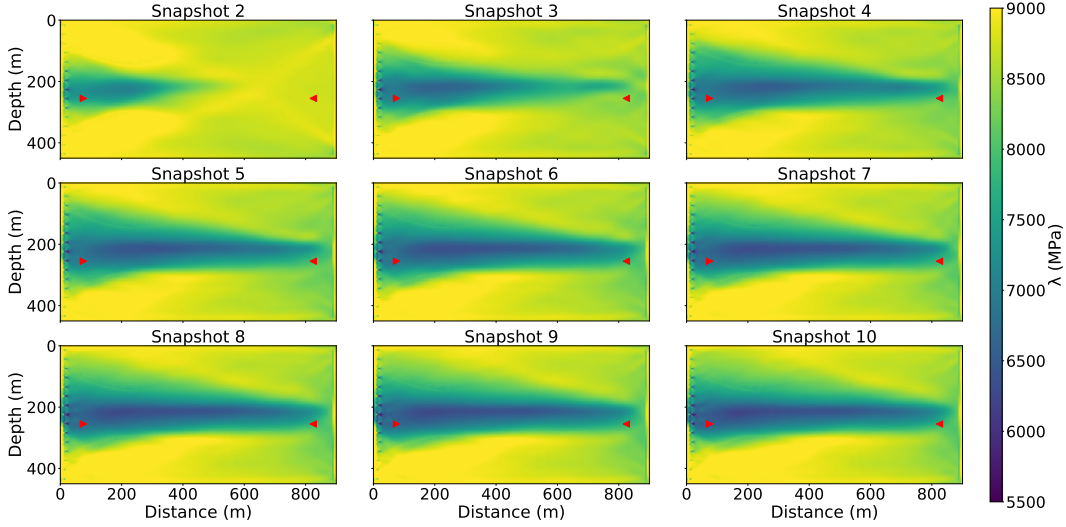


**Figure 7.** Inverted Lamé parameter  $\lambda$  for nine different surveys. The inversion is conducted using FWI with the same data separately for each survey. The survey configurations are the same as the baseline case.

model from coupled inversion (Fig. 8(a)), the permeability model from decoupled inversion is heavily contaminated with artifacts, although we can still identify the highly permeable layer. This model provides misleading information and would be harder to interpret. Also, the inverted model has a much larger MSE (1372.24) than the base case (MSE = 218.71). This experiment demonstrates the advantage and necessity of performing the coupled inversion.

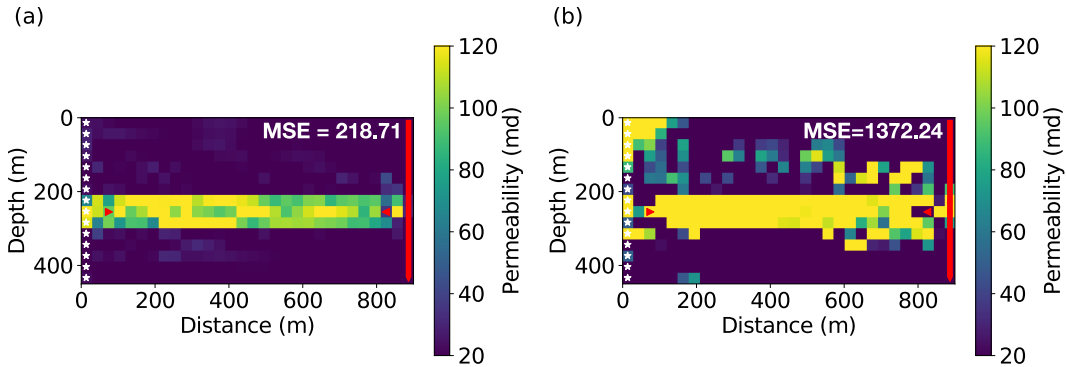


**Figure 8.** Comparison of inverted permeability model using (a) coupled inversion (baseline, MSE = 218.71), and (b) using  $\lambda$  separately inverted as shown in Fig. 7 (MSE = 1372.24). The separately fitted permeability model has much stronger artifacts and much larger MSE.

The inverted intrinsic properties can be used to predict flow behavior and also help reservoir management and optimization. With the inverted models from both the coupled and decoupled inversion strategy, we perform forward simulations of the flow and convert saturation maps to P-wave velocity maps. Fig 9(a) shows the predicted P-wave velocity evolution in slow time with the coupled inversion result, while Fig 9(b) shows the snapshots with the decoupled inversion result. The former one

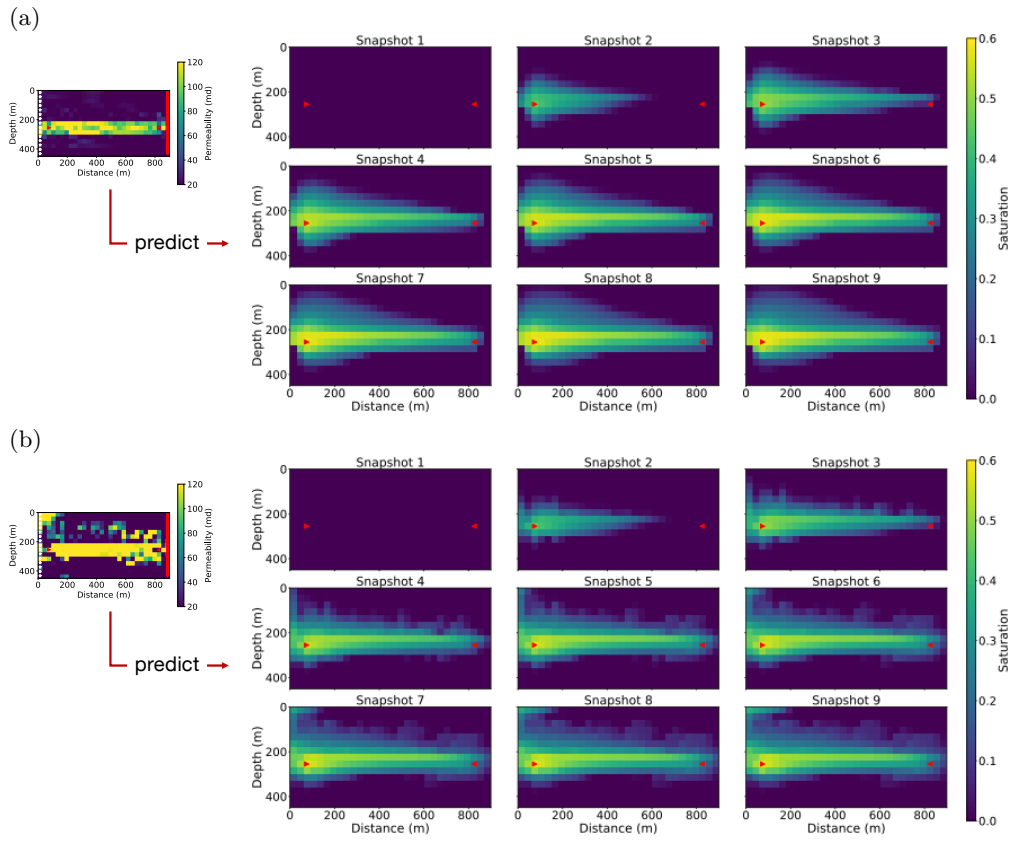


**Figure 9.** Predicted CO<sub>2</sub> saturation with models from (a) coupled and (b) decoupled (traditional) inversion. There are strong artifacts in the predicted snapshots in (b).

better predictions that are closer to the ground truth (Fig. 4) while the latter one leads to erroneous predictions with strong artifacts.

## 4.2 Inversion of Rock Physics Parameters

The rock physics model is a type of closure relationship that is sometimes empirical. We want to examine whether our method can also provide insight on calibration or discovery of such relationships. Therefore, we switched the rock physics model from the patchy saturation model to Gassmann’s model with Brie’s fluid mixture equation. The patchy saturation model is the upper bound of responses of elastic properties to fluid substitution. The Brie model introduced in Appendix A22, on the other hand, can approximate a wide range of rock physics models parameterized with the coefficient  $e$ . We plot the P-wave velocity of rocks against the saturation of CO<sub>2</sub> with the same parameters in previous numerical experiments. As is shown in Fig. (10),  $V_p$  drops first and then increases as the saturation of CO<sub>2</sub> increases in the Brie model, and as the coefficient  $e$  decreases, the curve gradually approximates the upper bound, a straight-line predicted by the patchy saturation model.

In the inversion experiments, the true rock physics model was assumed to be the Brie model with  $e = 3$ . We first used the exact rock physics model and Fig. 11(a) shows the inversion result, which has comparable accuracy as that from the patchy saturation model, with a low MSE equals 250.64. This result relies on the accurate assumption of rock physics models. However, if we have little information about the true rock physics model and wrongly assume that  $e = 2$ , Fig. 11(b) shows the inverted result that has much stronger artifacts and much higher MSE (2098.02). To mitigate such a common problem, we invert for the Brie’s coefficient  $e$  and permeability simultaneously. Thanks to the automatic differentiation capability of the framework, the gradient of the misfit function with respect to  $e$  can be easily obtained. The initial guess of  $e$  was also 2 as the previous experiment. Considering the range of value of the  $e$  coefficient is different from that of the permeability, we scaled up the value of  $e$  parameter by 30 and divided it by 30 before feeding it to the rock physics equations. Fig. 11(c) shows the inverted permeability with  $e$  updated simultaneously, which is more accurate (MSE = 320.04) than the previous case without updating. We show the inversion history of the  $e$  coefficient in Fig. 11(d), which quickly converges to the true  $e = 3$  after around 40 iterations. The initial drop of the value at the beginning several iterations are probably caused by the fact that the L-BFGS-B optimizer essentially acts as a gradient-descent at the beginning, which cannot handle the scaling of different parameters of different physical meanings well. This phenomenon was severe without the scaling trick that we just mentioned. In Fig. 11(e), we observe good convergence in data misfit of the simultaneous inversion. This promising result not only presents the multi-parameter inversion capability enabled by the automatic differentiable computing but also emphasizes that the simultaneous inversion can yield more accurate inversion results and provide insights on empirical relationships in practice.

## 4.3 A 2-D Stream Channel Model

In addition to the 3-layer model of horizontal layers, we also tested the coupled inversion for a stream channel model shown in Fig. 12(a), where the channel has a permeability of 120 md while the background is 20 md. This example can represent a vertical slice between vertical wells or a horizontal slice between horizontal wells.

This model has the same dimension as the 3-layer model, but has a smaller grid size of 5 m in both the vertical and horizontal directions, hence the model is parameterized by  $90 \times 180$  cells. We used this discretized model to create synthetic observed data. The synthetic saturation evolution maps for this channel model is shown in Fig. 13 for nine snapshots in slow-time. For the inversion, we increase the grid



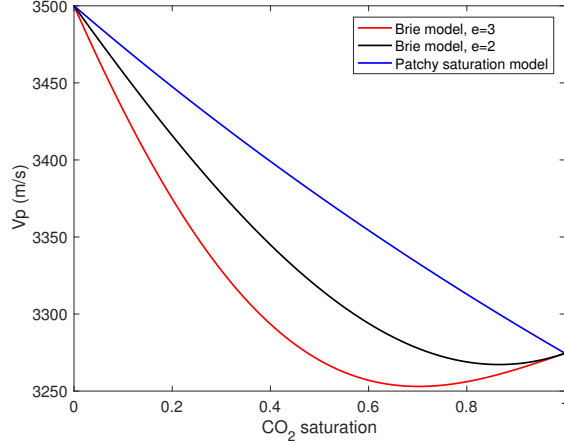


**Figure 10.** The  $V_p$ -saturation curve of the patchy saturation model, and the Gassmann’s model with Brie’s fluid mixture equations with different coefficients ( $e = 2$  and  $e = 3$ ).

size to 10 m yielding a grid of  $45 \times 90$  cells. The initial model is a homogeneous model of permeability of 20 md as previous experiments. Fig. 12(b) show the inversion result with data from 11 surveys after 100 iterations, which is the same all-at-once strategy as previous experiments. The 2-D channel is well reconstructed, meaning that our algorithm can also resolve complex 2-D structures with denser parameterization. The artifacts seen can be reduced by geological parameterization (Landa et al., 1997), or regularization methods (Aster et al., 2013; D. Li & Harris, 2018).

In real-world operations, it would be rare to wait and begin data analysis after completion of all surveys. Instead, it is a more practical strategy to perform continuous inversion along with new data from continuing surveys. In other words, at the end of survey  $i$  ( $i \geq 2$ ), we formulate an optimization/inversion problem with all available data so far  $\mathbf{d}_j^{\text{obs}}$  ( $j = 1, \dots, i$ ) and use the model from the previous stage of inversion as the initial model. We also tested the new strategy in this case. After a continuous inversion of only 6 surveys, we did not observe further improvement on the inversion result and report the inverted permeability model in Fig. 12(c), which seems to have fewer artifacts and lower MSE than that from the all-at-once strategy. Instead of inverting for all parameters at the same time, the continuous inversion strategy breaks the original problem into progressive bits, and it is easier to reconstruct the permeability field incrementally. Also, an accurate estimation of the flow properties at an early stage largely determines the accuracy of the following inversions due to the underline physics model.

## 5 Discussion & Conclusions

We have presented a novel approach for estimating intrinsic rock parameters such as permeability from time-lapse full-waveform inversion of geophysical data such as seismic. We demonstrated that solving an inverse problem constrained by coupled physical systems is superior to a decoupled inversion in terms of accuracy. Also, the method is effective in inverting an empirical rock physics model while estimating the subsurface permeability map at the same time.

We presented an intelligent automatic differentiation strategy for inversion. This strategy combines different levels of control over gradient computation schemes: customized PDE operators for time step marching in solving the flow equations, built-in

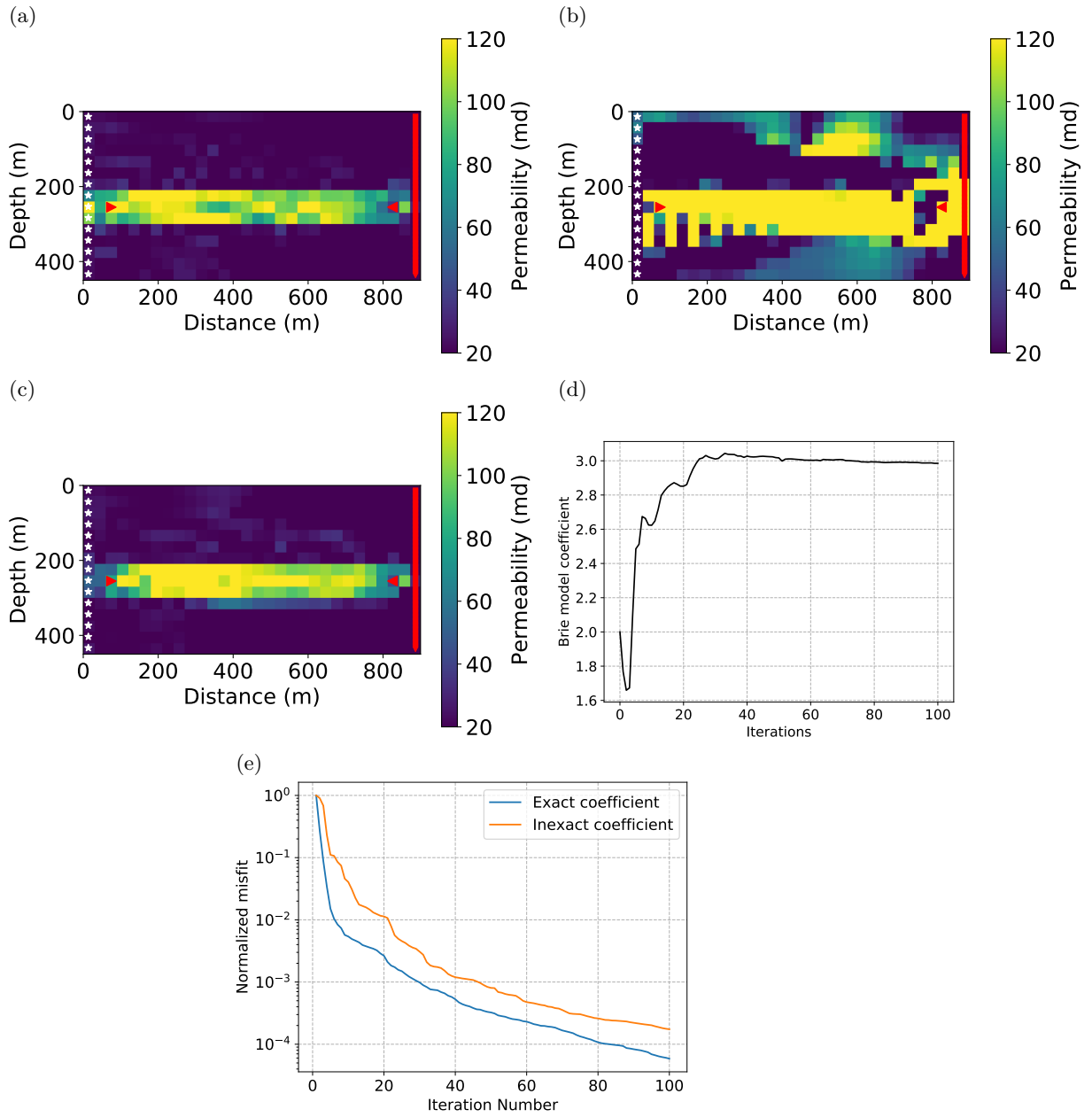


**Figure 11.** The inversion results with the Brie model. (a) Inverted permeability with the exact coefficient ( $e=3$ ); (b) Inverted permeability with incorrect coefficient ( $e=2$ ); (c) Inverted permeability with incorrect initial coefficient ( $e=2$ ) which is updated simultaneously; (d) The evolution of the value of  $e$  with iterations; (e) The convergence curves of the objective function for both cases.

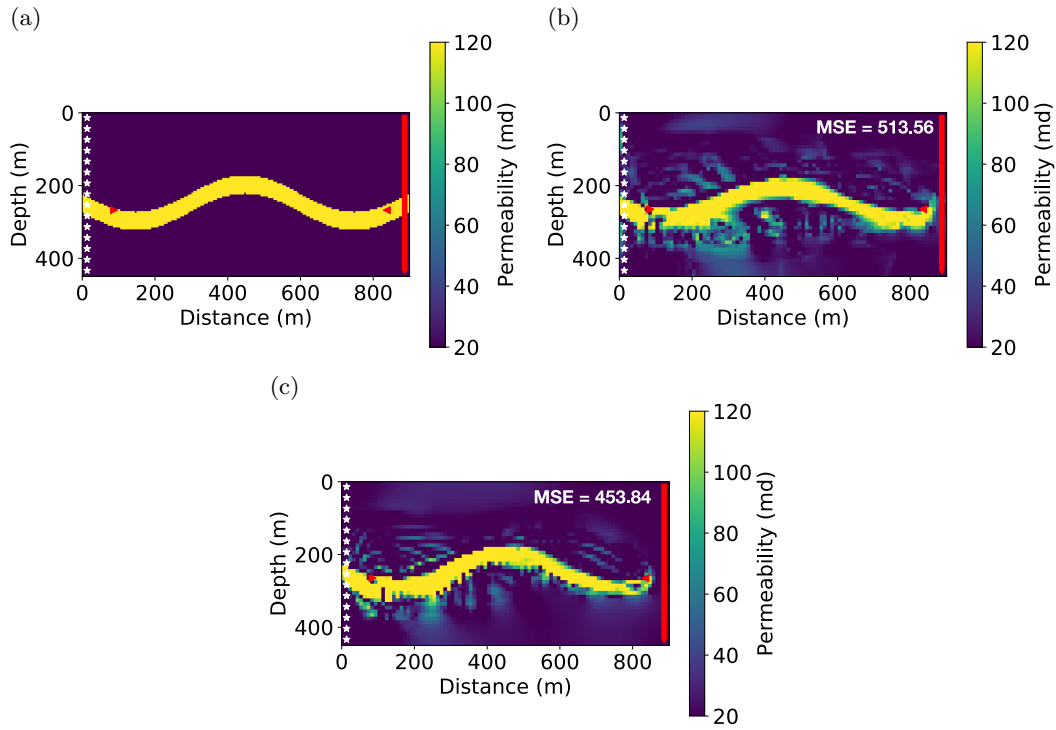


**Figure 12.** The inversion results of a channel model. (a) The true permeability model; (b) the inverted permeability model with the all-at-once inversion strategy; (c) the inverted permeability model with the continuous inversion strategy. The initial model is homogeneous with 20 md permeability as previous experiments.

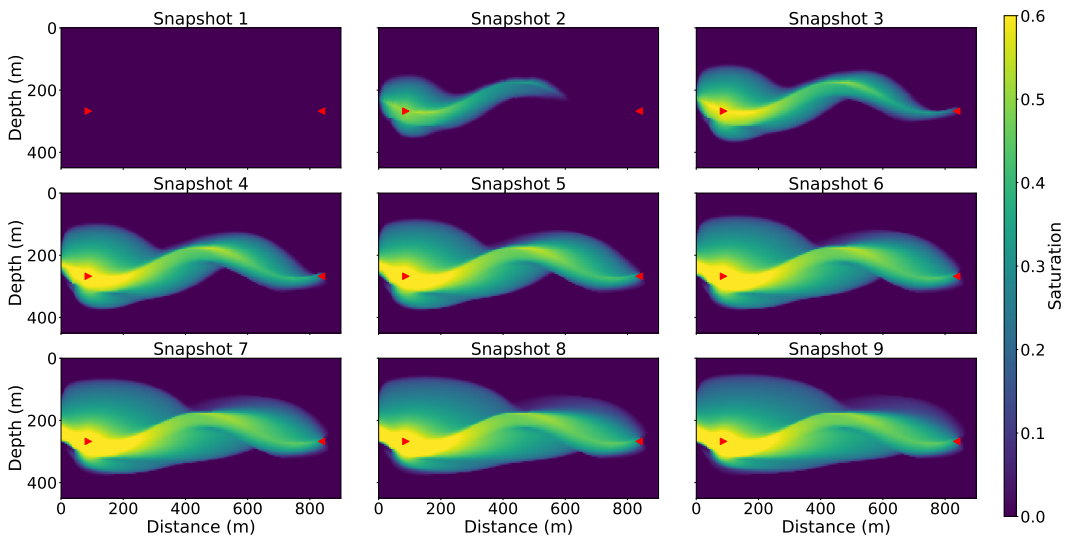


**Figure 13.** The first 9 snapshots of CO<sub>2</sub> saturation evolution of the channel model.

differentiable operators from `TensorFlow` for the rock physics models, and the discrete adjoint method for wave physics. With this strategy, we can fully exploit the power of modern machine learning platforms, and also make computations more efficient when necessary with algebraic multi-grid fast solvers, the Newton-Raphson method, an optimized GPU-accelerated FWI module, and in general various memory-saving techniques.

The applications of the intelligent automatic differentiation framework are by no means limited to the specific problem of fluid flow or CO<sub>2</sub> storage. To facilitate further research, we release the codes for this specific project

<https://github.com/lidongzh/FwiFlow.jl>

and the library codes at

<https://github.com/kailaix/ADCME.jl>

Some work remains to be done for inverse modeling with coupled PDE systems and hidden dynamics of subsurface flow. First, the rock physics conversion requires accurate reference elastic properties, on which elastic properties are based and altered by fluid substitution. Inaccurate reference properties may lead to non-physical elastic properties at subsequent survey times, making it difficult to fit the physics-based PDEs. Thus, we strongly advise one to estimate the reference properties as accurately as possible before subsequent time-lapse inversion. Also, the so-called “e factor” may for example depend on lithology. Second, seismic wave attenuation effects may be significant in flow-related problems. We can incorporate viscoelastic effects in wave physics modeling and expand elastic properties to anelastic properties, thus exploiting more wave physics behavior for flow inversion problems. Third, the gradient computation within the framework of automatic differentiation, which `ADCME` is based on, requires storing intermediate results for gradient back-propagation. In some situations, this will place excessive pressure on memory requirements. Check-pointing schemes can be used to alleviate this problem but require additional effort to implement. Finally, we must exercise care when interpreting the calibrated permeability or other hidden intrinsic parameters. If the flow has not reached certain areas throughout the slow time, the objective function has no sensitivity to flow parameters in those areas.

These questions form a promising line of future research. While our extensive numerical investigation shows the applicability and effectiveness of this novel approach, answering these questions is critical for deeper understanding and more practical applications. One such focused area we are pursuing is the investigation of the robustness of our coupled physics and intelligent AD approach to sparse datasets, that is, sparsity in space and slow-time. This problem is essential when continuous subsurface monitoring strategies are needed, and full datasets are expensive to record at each slow-time step. Finally, we note that our approach, demonstrated here in 2-D, is fully expandable to 3-D and as well to other seismic survey geometries.

## Appendix A More Details on the Physics Models

### A1 The Flow Physics Model

To solve the flow equations, we define the potentials of each phase as

$$\Psi_i = P_i - \rho_i g Z, \quad i = 1, 2, \tag{A1}$$

as well as the capillary potential

$$\Psi_c = P_c - (\rho_1 - \rho_2) g Z. \tag{A2}$$

We ignore the capillary pressure but retain the gravity term, hence  $\Psi_c = -(\rho_1 - \rho_2)gZ$ .

With the assumption of incompressibility and immiscibility of the fluids, and Eq. (10) and Eq. (11), we can obtain the following potential equation,

$$-\nabla \cdot (m_t K \nabla \Psi_2) = \nabla \cdot (m_1 K \nabla \Psi_c) + q, \quad (\text{A3})$$

where  $q = q_1 + q_2$ , where  $q_1$  and  $q_2$  are injection/production rate of fluid phase 1 and 2, respectively. With  $\Psi_\alpha$ , we can compute  $v_\alpha$ , and obtain the saturation equation as,

$$\phi \frac{\partial S_2}{\partial t} - \nabla \cdot (m_2 K \nabla \Psi_2) = q_2 \quad (\text{A4})$$

Hence, we have decoupled the original system of equations into two sub-equations and can solve them alternatively. Note that if we keep the production rate of fluid 1 as  $q_1$  and if the capillary pressure is zero, the injection/production rate of fluid 2 is  $q_2(\mathbf{x}, t) + q_1(\mathbf{x}, t) \frac{m_2(\mathbf{x}, t)}{m_1(\mathbf{x}, t)}$ , which means at the production well fluid 2 is also produced in proportion to fluid 1.

We adopt the no-flow boundary condition which reads as,

$$\mathbf{v}_i \cdot \mathbf{n} = 0, i = 1, 2, \quad (\text{A5})$$

where  $\mathbf{n}$  is the outward unit normal vector on the boundary. To apply this condition to our system, we define another two velocities as,

$$\mathbf{v}_t = -m_t K \nabla \Psi_2 \quad (\text{A6})$$

$$\mathbf{v}_c = -m_1 \nabla \Psi_c. \quad (\text{A7})$$

One can verify that  $\mathbf{v}_1 + \mathbf{v}_2 = \mathbf{v}_t + \mathbf{v}_c$ , and  $\mathbf{v}_2 = m_2 \mathbf{v}_t$ , from which we deduce that

$$\mathbf{v}_t \cdot \mathbf{n} = 0, \text{ and } \mathbf{v}_c \cdot \mathbf{n} = 0. \quad (\text{A8})$$

Therefore, for the potential equation, the boundary conditions are

$$\mathbf{n} \cdot \nabla \Psi_2 = 0, \text{ and } \mathbf{n} \cdot \nabla \Psi_c = 0. \quad (\text{A9})$$

It is insufficient to solve the potential equation (a Poisson's equation) only with the above Neumann boundary conditions; thus, we prescribe a Dirichlet boundary condition by forcing the potential to be a specific value at one point of the boundary.

## A2 Rock Physics Models

### A21 Patchy Saturation Model

If we have an estimation of P- and S-wave velocities and rock density before injection ( $C_{p1}$ ,  $C_{s1}$  and  $\rho_{r1}$ ), we can compute the bulk modulus  $B_{r1}$  and shear modulus  $\mu$  for rock fully saturated with fluid 1:

$$B_{r1} = \rho_{r1} \left( C_{p1}^2 - \frac{4}{3} C_{s1}^2 \right), \quad (\text{A10})$$

and

$$\mu = \rho_{r1} C_{s1}^2. \quad (\text{A11})$$

The patchy saturation model is suitable for the situation in which different fluids form isolated patches with a scale much larger than the pore space. The rock is stiffer than the case where fluids are well mixed in pore spaces. In the patchy saturation model, we first compute the bulk modulus of rock fully saturated with fluid 2 ( $B_{r2}$ ) by solving

$$\frac{B_{r2}}{B_o - B_{r2}} = \frac{B_{r1}}{B_o - B_{r1}} - \frac{B_{f1}}{\phi (B_o - B_{f1})} + \frac{B_{f2}}{\phi (B_o - B_{f2})}. \quad (\text{A12})$$

Then, the bulk modulus of partially saturated rock as a function of saturation of fluid 2 is

$$B_r(S_2) = \left[ (1 - S_2) \left( B_{r1} + \frac{4}{3}\mu \right)^{-1} + S_2 \left( B_{r2} + \frac{4}{3}\mu \right)^{-1} \right]^{-1} - \frac{4}{3}\mu. \quad (\text{A13})$$

Since the shear modulus of fluids is zero, we assume that the rock shear modulus does not change with  $S_2$  replacing  $S_1$ . Therefore, the first Lamé parameter  $\lambda$  is

$$\lambda(S_2) = B(S_2) - \frac{2}{3}\mu. \quad (\text{A14})$$

To calculate density, we note that the densities of rock fully saturated with fluid 1 ( $\rho_{r1}$ ) and with fluid 2 ( $\rho_{r2}$ ) have the following relationship

$$\begin{cases} \rho_{r1} = \rho_o(1 - \phi) + \phi\rho_1 \\ \rho_r(S_2) = \rho_o(1 - \phi) + \phi[(1 - S_2)\rho_1 + S_2\rho_2], \end{cases} \quad (\text{A15})$$

where  $S_2$  is the saturation of fluid 2,  $\rho_o$  denotes the density of rock grains,  $\rho_i$ , ( $i = 1, 2$ ) are the density of fluid 1 and 2, respectively. Thus, we obtain the rock density as a function of the saturation of fluid 2 as

$$\rho(S_2) = \rho_{r1} + \phi S_2(\rho_2 - \rho_1). \quad (\text{A16})$$

With the elastic properties  $\lambda$ ,  $\mu$  and  $\rho$ , we compute the elastic wavefield with Eq. (17).

### ***A22 Gassmann's Model with Brie's Fluid Mixing Equation***

Gassmann's model with Brie's fluid mixing equation (Brie et al., 1995) is an empirical relationship that is able to describe the situation where two types of fluids are not completely segregated in patches. In Gassmann's model, the first step is to compute the bulk modulus of mixed fluid  $K_{f\_mix}$ :

$$B_{f\_mix} = (B_{f1} - B_{f2})(1 - S_2)^e + B_{f2}, \quad (\text{A17})$$

where  $e$  is the Brie model coefficient. The second step is to use Gassmann's equation to compute the bulk modulus of the rock partially saturated with fluid 2  $B_r(S_2)$ :

$$\frac{B_r}{B_o - B_r} = \frac{B_{r1}}{B_o - B_{r1}} - \frac{B_{f1}}{\phi(B_o - B_{f1})} + \frac{B_{f\_mix}}{\phi(B_o - B_{f\_mix})}. \quad (\text{A18})$$

If  $e = 1$ , it is close to the patch saturation model, and if  $e$  is substantially large the model behaves like the Gassmann model with the Reuss average of fluids (Mavko et al., 2009). Usually,  $e$  is chosen as 3. As we see in Section 4.2 that with the Gassmann's model, rock P-wave velocity drops more quickly at the beginning of CO<sub>2</sub> injection and increases later because of the decrease in density; while in the patchy saturation model, rock P-wave velocity almost follows a straight line against CO<sub>2</sub> saturation. Although this is an empirical closure relationship, we show in Section 4.2 that it is also possible to update the coefficient  $e$  simultaneously with intrinsic parameter inversion.

## **Appendix B Discrete Adjoint Method**

The adjoint method is an effective technique to derive gradients for large-scale PDE-constrained inverse problems, such as full-waveform inversion, history matching (Oliver & Chen, 2011; R. Li et al., 2001), 4D variational weather data assimilation (Wang et al., 2001), ocean model inversion (Marotzke et al., 1999), etc. Our inversion method is also based on the adjoint method, which we briefly introduce here.

Consider an inverse problem of the following form:

$$\begin{aligned} \min_{\boldsymbol{\theta}} \mathcal{J}(\mathbf{u}(\boldsymbol{\theta})) \\ \text{s.t. } \mathcal{A}(\mathbf{u}(\boldsymbol{\theta}), \boldsymbol{\theta}) = 0, \end{aligned} \quad (\text{B1})$$

where  $J$  is a functional of  $\mathbf{u}$ , which is obtained by solving a differential equation  $\mathcal{A}(\mathbf{u}, \boldsymbol{\theta}) = 0$ . The constraint either explicitly or implicitly establishes that  $\mathbf{u}$  is a function of  $\boldsymbol{\theta}$ , the unknown parameter to be solved for. To solve this problem, one may use the method of Lagrange multipliers to transform this constrained problem into an unconstrained problem as

$$\min_{\boldsymbol{\theta}, \mathbf{u}} \max_{\boldsymbol{\lambda}} \mathcal{L}(\boldsymbol{\theta}, \mathbf{u}, \boldsymbol{\lambda}) = \mathcal{J}(\mathbf{u}) + \boldsymbol{\lambda}^T \mathcal{A}(\mathbf{u}, \boldsymbol{\theta}). \quad (\text{B2})$$

According to the KKT condition, the necessary condition for achieving an optimum is

$$\frac{\partial \mathcal{L}}{\partial \boldsymbol{\theta}} = 0, \quad \frac{\partial \mathcal{L}}{\partial \mathbf{u}} = 0, \quad \frac{\partial \mathcal{L}}{\partial \boldsymbol{\lambda}} = 0 \quad (\text{B3})$$

Although one may update  $\boldsymbol{\theta}$ ,  $\mathbf{u}$ , and  $\boldsymbol{\lambda}$  simultaneously using methods such as gradient descent plus dual ascent until they satisfy condition (B3), it is more common and feasible to require that the KKT condition for both  $\mathbf{u}$  and  $\boldsymbol{\lambda}$  is satisfied throughout the optimization process. The latter strategy is the so-called adjoint method. In other words, we have

$$\frac{\partial \mathcal{L}}{\partial \boldsymbol{\lambda}} = \mathcal{A}(\mathbf{u}, \boldsymbol{\theta}) = 0 \quad (\text{B4})$$

$$\frac{\partial \mathcal{L}}{\partial \mathbf{u}} = \mathcal{J}_{\mathbf{u}} + \boldsymbol{\lambda}^T \mathcal{A}_{\mathbf{u}} = 0. \quad (\text{B5})$$

The first equation is just the normal PDE constraint where we solve for  $\mathbf{u}$ , while the second is the adjoint equation from which we can find the Lagrange multiplier or dual variable  $\boldsymbol{\lambda}$  once we have obtained  $\mathbf{u}$ . One uses

$$\frac{d\mathcal{J}}{d\boldsymbol{\theta}} = \frac{\partial \mathcal{L}}{\partial \boldsymbol{\theta}} = \boldsymbol{\lambda}^T \mathcal{A}_{\boldsymbol{\theta}}, \quad (\text{B6})$$

to calculate the gradient of the objective function to the parameter and then use gradient-based optimization methods to solve the problem. Note that the first equality of Equation (B6) comes from the fact that we keep  $\mathcal{A}(\mathbf{u}, \boldsymbol{\theta}) = 0$  as in Eq. (B4). We also point out that we adopt the discretize-then-optimize strategy. Namely, we discrete the constraint PDE first and then derive the discrete adjoint equation and gradient. It is easier to obtain a numerically exact gradient in this way.

One interesting fact deduced from Eq. (B5) is that the adjoint equation is always linear, despite that the forward equation may be nonlinear.

In Appendix D, we demonstrate how to apply the discretized-adjoint method to the first-order elastic wave equation system with the CPML boundary condition.

## Appendix C The connection between Automatic Differentiation and the Discrete Adjoint Method

Let us consider a simplified inverse problem for slow-time processes illustrated in Fig. C1. The nodes are variables, and arrows indicate operations. The property  $\mathbf{u}$  evolves from the initial condition  $\mathbf{u}_1$  to  $\mathbf{u}_4$ , whose behavior is also controlled by the parameter  $\boldsymbol{\theta}$ . We may decompose the mapping into sequential steps such as  $f_1, \dots, f_4$ . The last operator  $f_4$  computes the objective function  $\mathcal{J}$ . Mathematically, the mappings are written as

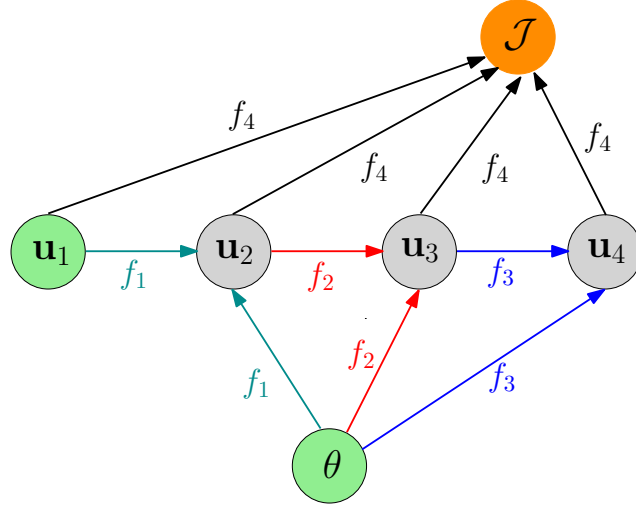


**Figure C1.** The computational graph of simplified slow-time process inversion.  $\mathbf{u}_1$  and  $\theta$  are the input vectors,  $J$  is the output scalar, and  $\mathbf{u}_2$ ,  $\mathbf{u}_3$ , and  $\mathbf{u}_4$  are intermediate variables.

$$\begin{aligned}
 \mathbf{u}_2 &= f_1(\mathbf{u}_1, \theta) \\
 \mathbf{u}_3 &= f_2(\mathbf{u}_2, \theta) \\
 \mathbf{u}_4 &= f_3(\mathbf{u}_3, \theta) \\
 J &= f_4(\mathbf{u}_1, \mathbf{u}_2, \mathbf{u}_3, \mathbf{u}_4).
 \end{aligned} \tag{C1}$$

Then, we construct the following inverse problem,

$$\begin{aligned}
 \min_{\mathbf{u}_1, \theta} & f_4(\mathbf{u}_1, \mathbf{u}_2, \mathbf{u}_3, \mathbf{u}_4), \\
 \text{s.t.} & \mathbf{u}_2 = f_1(\mathbf{u}_1, \theta), \\
 & \mathbf{u}_3 = f_2(\mathbf{u}_2, \theta), \\
 & \mathbf{u}_4 = f_3(\mathbf{u}_3, \theta).
 \end{aligned} \tag{C2}$$

Following the adjoint method in Section Appendix B, we obtain the Lagrangian as

$$\mathcal{L} = f_4(\mathbf{u}_1, \mathbf{u}_2, \mathbf{u}_3, \mathbf{u}_4) + \lambda_2^T (f_1(\mathbf{u}_1, \theta) - \mathbf{u}_2) + \lambda_3^T (f_2(\mathbf{u}_2, \theta) - \mathbf{u}_3) + \lambda_4^T (f_3(\mathbf{u}_3, \theta) - \mathbf{u}_4) \tag{C3}$$

Taking the derivate of  $\mathcal{L}$  with respect to  $\mathbf{u}_i$  and  $\theta$ , and setting them to zero yields

$$\begin{aligned}
 \lambda_4^T &= \frac{\partial f_4}{\partial \mathbf{u}_4} \\
 \lambda_3^T &= \frac{\partial f_4}{\partial \mathbf{u}_3} + \lambda_4^T \frac{\partial f_3}{\partial \mathbf{u}_3} \\
 \lambda_2^T &= \frac{\partial f_4}{\partial \mathbf{u}_2} + \lambda_3^T \frac{\partial f_2}{\partial \mathbf{u}_2} \\
 \frac{\partial \mathcal{L}}{\partial \theta} &= \lambda_2^T \frac{\partial f_1}{\partial \theta} + \lambda_3^T \frac{\partial f_2}{\partial \theta} + \lambda_4^T \frac{\partial f_3}{\partial \theta} \rightarrow 0.
 \end{aligned} \tag{C4}$$

We can recognize that the Lagrange multipliers or adjoint variable  $\lambda_i^T = \frac{\partial J}{\partial \mathbf{u}_i}$ ,  $i = 2, 3, 4$ ; that is, they are the partial derivative of the objective respect to intermediate



variables. Eq. (C4) “back-propagate” or “spray”  $\lambda_i$  to the parent nodes pointing to node  $i$ , followed by multiplications such as  $\lambda_4^T \frac{\partial f_3}{\partial \theta}$ .

This is exactly the same “back-propagation” scheme in the reverse-mode automatic differentiation, but AD is different in the programming interface, in which we only need to implement two methods for each customized operator:

1. Forward operation  $f_n$ : compute the output by solving a certain PDE.
2. Backward operation  $b_n$ : given gradient  $\frac{\partial \mathcal{J}}{\partial \mathbf{u}_{n+1}}$ , compute  $\frac{\partial \mathcal{J}}{\partial \mathbf{u}_{n+1}} \frac{\partial f_n}{\partial \mathbf{u}_n}$  and  $\frac{\partial \mathcal{J}}{\partial \mathbf{u}_{n+1}} \frac{\partial f_n}{\partial \theta}$  with the chain rule. Note that only a matrix-vector product needs to be implemented, and there should be no need to construct Jacobian matrices like  $\frac{\partial f_n}{\partial \mathbf{u}_n}$  explicitly.

$$\frac{\partial \mathcal{J}}{\partial \mathbf{u}_{n+1}} \frac{\partial f_n}{\partial \mathbf{u}_n}, \quad \frac{\partial \mathcal{J}}{\partial \mathbf{u}_{n+1}} \frac{\partial f_n}{\partial \theta} = b_n \left( \frac{\partial \mathcal{J}}{\partial \mathbf{u}_{n+1}}, \mathbf{u}_{n+1}, \mathbf{u}_n, \theta \right) \quad (\text{C5})$$

## Appendix D Discretization of the Wave Equation & Derivation of Its Adjoint System and Gradients

We use operator  $D_z^+, D_x^+$  and  $D_z^-, D_x^-$  to denote the fourth-order staggered grid finite difference operators in either  $z$  axis or  $x$  axis. The plus sign means that the finite difference is forward, while the minus sign means backward. For example,

$$\begin{aligned} D_z^+ c_{ij} &:= \left[ \frac{9}{8} (c_{i+1,j} - c_{i,j}) - \frac{1}{24} (c_{i+2,j} - c_{i-1,j}) \right] \frac{1}{\Delta z} \\ D_z^- c_{ij} &:= \left[ \frac{9}{8} (c_{i,j} - c_{i-1,j}) - \frac{1}{24} (c_{i+1,j} - c_{i-2,j}) \right] \frac{1}{\Delta z} \end{aligned} \quad (\text{D1})$$

The staggered grid layout is illustrated in Figure D1, which features the configuration of wavefield variables and elastic parameters in the  $ij$ -th cell.

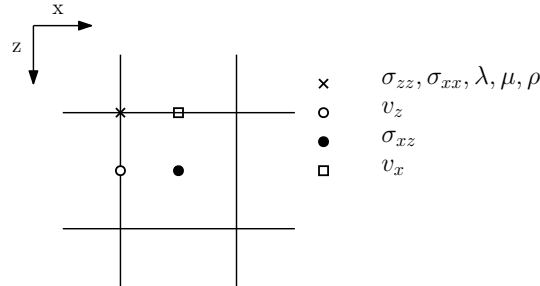


**Figure D1.** Cell  $(i, j)$  of the staggered-grid for elastic wave equation. We define particle velocity components  $v_z, v_x$ , stress tensor components  $\sigma_{zz}, \sigma_{xx}, \sigma_{xz}$  and elastic parameters  $\lambda, \mu, \rho$  of spatial index  $(i, j)$  in the annotated locations.

The discretized elastic wave equation with CPML boundary condition is

$$\begin{aligned}
 \varphi_{zz}^{t+1} - b_z \varphi_{zz}^t - a_z D_z^- V_z^t &= 0 \\
 \varphi_{xx}^{t+1} - b_x \varphi_{xx}^t - a_x D_x^- V_x^t &= 0 \\
 S_{zz}^{t+1} - S_{zz}^t - (\lambda + 2\mu) \left[ \frac{1}{K_z} D_z^- V_z^t + \varphi_{zz}^{t+1} \right] \Delta t - \lambda \left[ \frac{1}{K_x} D_x^- V_x^t + \varphi_{xx}^{t+1} \right] \Delta t - c_z f^t \Delta t &= 0 \\
 S_{xx}^{t+1} - S_{xx}^t - \lambda \left[ \frac{1}{K_z} D_z^- V_z^t + \varphi_{zz}^{t+1} \right] \Delta t - (\lambda + 2\mu) \left[ \frac{1}{K_x} D_x^- V_x^t + \varphi_{xx}^{t+1} \right] \Delta t - c_x f^t \Delta t &= 0 \\
 \varphi_{xz}^{t+1} - b_{zh} \varphi_{xz}^t - a_{zh} D_z^+ V_x^t &= 0 \\
 \varphi_{zx}^{t+1} - b_{xh} \varphi_{zx}^t - a_{xh} D_x^+ V_z^t &= 0 \\
 S_{xz}^{t+1} - S_{xz}^t - \mu_{\text{ave}} \left[ \frac{1}{K_{zh}} D_z^+ V_x^t + \varphi_{xz}^{t+1} + \frac{1}{K_{xh}} D_x^+ V_z^t + \varphi_{zx}^{t+1} \right] \Delta t &= 0 \\
 \phi_{zz-z}^{t+1} - b_{zh} \phi_{zz-z}^t - a_{zh} D_z^+ S_{zz}^{t+1} &= 0 \\
 \phi_{xz-x}^{t+1} - b_x \phi_{xz-x}^t - a_x D_x^- S_{xz}^{t+1} &= 0 \\
 V_z^{t+1} - V_z^t - \left[ \frac{1}{K_{zh}} D_z^+ S_{zz}^{t+1} + \phi_{zz-z}^{t+1} + \frac{1}{K_x} D_x^- S_{xz}^{t+1} + \phi_{xz-x}^{t+1} \right] \frac{1}{\rho_a} \Delta t &= 0 \\
 \phi_{xz-z}^{t+1} - b_z \phi_{xz-z}^t - a_z D_z^- S_{xz}^{t+1} &= 0 \\
 \phi_{xx-x}^{t+1} - b_{xh} \phi_{xx-x}^t - a_{xh} D_x^+ S_{xx}^{t+1} &= 0 \\
 V_x^{t+1} - V_x^t - \left[ \frac{1}{K_z} D_z^- S_{xz}^{t+1} + \phi_{xz-z}^{t+1} + \frac{1}{K_{xh}} D_x^+ S_{xx}^{t+1} + \phi_{xx-x}^{t+1} \right] \frac{1}{\rho_b} \Delta t &= 0,
 \end{aligned} \tag{D2}$$

where the space index  $i, j$  is omitted for all variables for brevity. In other words,  $S_{zz}^{t+1}$  is a shorthand for  $S_{zz;i,j}^{t+1}$ . In this system of discretized PDEs,  $\varphi_{zz}, \varphi_{xx}, \varphi_{xz}, \varphi_{zx}$  are CPML memory variables for computing spatial derivatives of the particle velocities  $V_z, V_x$ . Similarly,  $\phi_{zz-z}, \phi_{xz-x}, \phi_{xz-z}, \phi_{xx-x}$  are CPML memory variables for computing spatial derivatives of the stress components  $S_{zz}, S_{xz}, S_{xx}$ . The CPML coefficient profiles  $b_z, b_x, a_z, a_x, K_z, K_x$  are defined in (Martin et al., 2008), and  $b_{zh}, b_{xh}, a_{zh}, a_{xh}, K_{zh}, K_{xh}$  are such coefficients shifted by half-grid due to the staggered-grid configuration. The coefficients  $c_z, c_x$  are the magnitudes of the normal stress components when implementing the borehole source. The density and shear modulus are averaged as follows:

1.  $\rho_a$  is the density at the circles:

$$\rho_{a;i,j} = \frac{1}{2}(\rho_{i,j} + \rho_{i+1,j}) \tag{D3}$$

2.  $\rho_b$  is the density at the boxes:

$$\rho_{b;i,j} = \frac{1}{2}(\rho_{i,j} + \rho_{i,j+1}) \tag{D4}$$

3.  $\mu_{\text{ave}}$  is the shear modulus at the black dots:

$$\mu_{\text{ave};i,j} = 4 / \left( \frac{1}{\mu_{\text{ave};i,j}} + \frac{1}{\mu_{\text{ave};i+1,j}} + \frac{1}{\mu_{\text{ave};i,j+1}} + \frac{1}{\mu_{\text{ave};i+1,j+1}} \right), \tag{D5}$$

and is set to zero when  $\mu$  at any of the four corners is zero.

To derive the discrete adjoint system, we formulate the Lagrangian as

$$\begin{aligned}
 \mathcal{L} = & \frac{1}{2} \sum_{r=1}^{N_r} \left[ d_r^{t+1} - (c_z \mathcal{Q}_r(S_{zz}^{t+1}) + c_x \mathcal{Q}_r(S_{xx}^{t+1})) \right]^2 \\
 & + \left\langle \tilde{\varphi}_{zz}^{t+1}, \varphi_{zz}^{t+1} - b_z \varphi_{zz}^t - a_z D_z^- V_z^t \right\rangle \\
 & + \left\langle \tilde{\varphi}_{xx}^{t+1}, \varphi_{xx}^{t+1} - b_x \varphi_{xx}^t - a_x D_x^- V_x^t \right\rangle \\
 & + \left\langle \tilde{S}_{zz}^{t+1}, S_{zz}^{t+1} - S_{zz}^t - (\lambda + 2\mu) \left[ \frac{1}{K_z} D_z^- V_z^t + \varphi_{zz}^{t+1} \right] \Delta t - \lambda \left[ \frac{1}{K_x} D_x^- V_x^t + \varphi_{xx}^{t+1} \right] \Delta t - c_z f^t \Delta t \right\rangle \\
 & + \dots \\
 & + \left\langle \tilde{V}_x^{t+1}, V_x^{t+1} - V_x^t - \left[ \frac{1}{K_z} D_z^- S_{xz}^{t+1} + \phi_{xz-z}^{t+1} + \frac{1}{K_{xh}} D_x^+ S_{xx}^{t+1} + \phi_{xx-x}^{t+1} \right] \frac{1}{\rho_b} \Delta t, \right\rangle
 \end{aligned} \tag{D6}$$

where the variables with a tilde are the adjoint wavefield variables or the Lagrange multipliers, and the large bracket denotes discrete inner product in space and time, and  $\mathcal{Q}$  is the sampling operator at receiver  $r$ .

Using the adjoint method, we obtain the adjoint equations

$$\begin{aligned}
 \tilde{V}_x^t - \tilde{V}_x^{t+1} + a_x D_x^+ \tilde{\varphi}_{xx}^{t+1} + \lambda \frac{1}{k_x} D_x^+ \tilde{S}_{zz}^{t+1} \Delta t + (\lambda + 2\mu) \frac{1}{k_x} D_x^+ \tilde{S}_{xx}^{t+1} \Delta t + a_{zh} D_z^- \tilde{\varphi}_{xz}^{t+1} + \mu_{\text{ave}} \frac{1}{k_{zh}} D_z^- \tilde{S}_{xz}^{t+1} \Delta t &= 0 \\
 \tilde{\phi}_{xx-x}^t - b_{xh} \tilde{\phi}_{xx-x}^{t+1} - \tilde{V}_x^t \frac{1}{\rho_b} \Delta t &= 0 \\
 \tilde{\phi}_{xz-z}^t - b_z \tilde{\phi}_{xz-z}^{t+1} - \tilde{V}_x^t \frac{1}{\rho_b} \Delta t &= 0 \\
 \tilde{V}_z^t - \tilde{V}_z^{t+1} + a_z D_z^+ \tilde{\varphi}_{zz}^{t+1} + (\lambda + 2\mu) \frac{1}{k_z} D_z^+ \tilde{S}_{zz}^{t+1} \Delta t + \lambda \frac{1}{k_z} D_z^+ \tilde{S}_{xx}^{t+1} \Delta t + a_{xh} D_x^- \tilde{\varphi}_{zx}^{t+1} + \mu_{\text{ave}} \frac{1}{k_{xh}} D_x^- \tilde{S}_{xz}^{t+1} \Delta t &= 0 \\
 \tilde{\phi}_{xz-x}^t - b_x \tilde{\phi}_{xz-x}^{t+1} - \tilde{V}_z^t \frac{1}{\rho_a} \Delta t &= 0 \\
 \tilde{\phi}_{zz-z}^t - b_{zh} \tilde{\phi}_{zz-z}^{t+1} - \tilde{V}_z^t \frac{1}{\rho_a} \Delta t &= 0 \\
 \tilde{S}_{xz}^t - \tilde{S}_{xz}^{t+1} + a_x D_x^+ \tilde{\phi}_{xz-x}^t + \frac{1}{k_x \rho_a} D_x^+ \tilde{V}_z^t \Delta t + a_z D_z^+ \tilde{\phi}_{xz-z}^t + \frac{1}{k_z \rho_b} D_z^+ \tilde{V}_x^t \Delta t &= 0 \\
 \tilde{\varphi}_{zx}^t - b_{xh} \tilde{\varphi}_{zx}^{t+1} - \tilde{S}_{xz}^t \mu_{\text{ave}} \Delta t &= 0 \\
 \tilde{\varphi}_{xz}^t - b_{zh} \tilde{\varphi}_{xz}^{t+1} - \tilde{S}_{xz}^t \mu_{\text{ave}} \Delta t &= 0 \\
 \tilde{S}_{xx}^t - \tilde{S}_{xx}^{t+1} + a_{xh} D_x^- \tilde{\phi}_{xx-x}^t + \frac{1}{k_{xh} \rho_b} D_x^- \tilde{V}_x^t \Delta t + c_x (c_z S_{zz}^t + c_x S_{xx}^t - d^t) &= 0 \\
 \tilde{S}_{zz}^t - \tilde{S}_{zz}^{t+1} + a_{zh} D_z^- \tilde{\phi}_{zz-z}^t + \frac{1}{k_{zh} \rho_a} D_z^- \tilde{V}_z^t \Delta t + c_z (c_z S_{zz}^t + c_x S_{xx}^t - d^t) &= 0 \\
 \tilde{\varphi}_{xx}^t - b_x \tilde{\varphi}_{xx}^{t+1} - \lambda \tilde{S}_{zz}^t \Delta t - (\lambda + 2\mu) \tilde{S}_{xx}^t \Delta t &= 0 \\
 \tilde{\varphi}_{zz}^t - b_z \tilde{\varphi}_{zz}^{t+1} - (\lambda + 2\mu) \tilde{S}_{zz}^t \Delta t - \lambda \tilde{S}_{xx}^t \Delta t &= 0
 \end{aligned} \tag{D7}$$

Note that the system is solved backwards in time. For example, the gradient of the objective function with respect to  $\lambda$  is

$$\nabla_{\lambda} \lambda_{i,j} = - \sum_{t=1}^{N_t} (\tilde{S}_{zz}^{t+1} + \tilde{S}_{xx}^{t+1}) (D_z^- V_{z;i,j}^t + D_x^- V_{x;i,j}^t) \Delta t, \tag{D8}$$

where  $N_t$  is the number of simulation steps.

## Appendix E An Example of Implementation of Customized PDE operators

We discuss the discretization and numerical implementation of forward modeling and gradient computation in this section. Since the discrete adjoint scheme for the elastic wave equation is discussed in Appendix D, we mainly focus on the implementation of the forward and backward methods for operators of a single time step in the two-phase flow equations.

### E1 Forward Operation

In the forward simulations, we solve the discretized potential equation and saturation equation at each time step  $n$ :

$$-\nabla \cdot (m_t(S_2^n) K \nabla \Psi_2^n) = \nabla \cdot (m_1(S_2^n) K \nabla \Psi_c(S_2^n)) + q^n, \quad (\text{E1})$$

$$\phi(S_2^{n+1} - S_2^n) - \nabla \cdot (m_2(S_2^{n+1}) K \nabla \Psi_2^n) \Delta t = \left( q_2^n + q_1^n \frac{m_2(S_2^{n+1})}{m_1(S_2^{n+1})} \right) \Delta t, \quad (\text{E2})$$

where the upper script  $n$  stands for time step  $n$ , and  $\Delta t$  denotes the interval of a single time step. We first solve for  $\Psi_2^n$  using  $S_2^n$ , and then we solve for  $S_2^{n+1}$  with the obtained  $\Psi_2^n$ . In the saturation equation, we adopt the backward-Euler time scheme, which means that saturation-dependent parameters in the equation are functions of the to-be-solved saturation at time  $n+1$  ( $S_2^{n+1}$ ). This makes the time-stepping scheme implicit, which has the advantage that it is unconditionally stable, and thus the time step can be large.

In actual implementations, we divide the whole processes into four sequential forward operators:

$$m_1, m_t, \Psi_c = f_{\text{op1}}(S_2^n) \quad (\text{E3})$$

$$\tilde{q}^n = f_{\text{op2}}(K, m_1, \Psi_c, q^n) \quad (\text{E4})$$

$$\Psi_2^n = f_{\text{op3}}(K, m_t, \tilde{q}^n) \quad (\text{E5})$$

$$S_2^{n+1} = f_{\text{op4}}(S_2^n, K, \Psi_2^n, \phi, q_2^n), \quad (\text{E6})$$

where the  $f_{\text{op1}}$  computes mobilities  $m_1, m_t$  and capillary potential  $\Psi_c$  based on  $S_2^n$ , the  $f_{\text{op2}}$  computes the right-hand side of the discretized potential equation (E1):

$$\tilde{q}^n = \nabla \cdot (m_1 K \nabla \Psi_c) + q^n, \quad (\text{E7})$$

the  $f_{\text{op3}}$  solves the Poisson equation from Eq. (E1):

$$-\nabla \cdot (m_t K \nabla \Psi_2^n) = \tilde{q}^n, \quad (\text{E8})$$

and finally  $f_{\text{op4}}$  solves the non-linear implicit discretized saturation equation (E2) with the Newton-Raphson method (Appendix F).

For the spatial discretization, we adopt a second-order finite difference scheme in a cell-center grid, which is equivalent to the two-point-flux finite volume method (Lie, 2019). Fig. E1 shows the computational grid, where the saturation, potential, and other parameters are allocated in the center of the cells. The grid intervals  $h$  of the cell in the  $z$  and  $x$  directions are the same, while in the  $y$ -direction perpendicular to the plane and the thickness of the cell is  $h_y$ .

The key to the spatial discretization of Eqs. (E1) and (E2) is the variable-coefficient Laplacian of the following form

$$\nabla \cdot (m K \nabla \Psi), \quad (\text{E9})$$

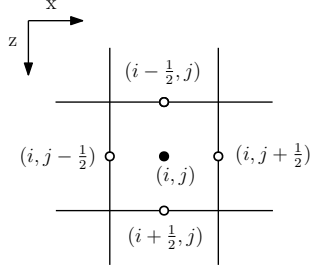


**Figure E1.** The cell-centered grid for two-phase flow equations. For cell  $(i, j)$  shown in the figure, quantities are defined in the central black dot. We interpolate those quantities at the half grid points illustrated by circles for computation of second-order derivatives at the black dots. The grid intervals in the  $z$  and  $x$  directions are the same. The cell has a thickness of  $h_y$ .

where  $m$  can be  $m_1, m_2$  or  $m_t$ , and  $\Psi$  can be  $\Psi_2^n$  or  $\Psi_c$ .

The  $z$  and  $x$  components of  $\nabla\Psi$  are defined on half grid points, since  $\Psi_{i,j}$  are defined on cell centers. Therefore, we need to interpolate mobility  $m$  and permeability  $K$  onto half grid points. We use the harmonic average of permeabilities in the two adjacent cells as the permeability at half grid points:

$$\begin{aligned} K_{i,j+\frac{1}{2}} &= \frac{K_{i,j} K_{i,j+1}}{K_{i,j} + K_{i,j+1}} \\ K_{i+\frac{1}{2},j} &= \frac{K_{i,j} K_{i+1,j}}{K_{i+1,j} + K_{i,j}}. \end{aligned} \quad (\text{E10})$$

As for mobilities  $m$ , we adopt the upwind scheme:

$$\begin{aligned} m_{i,j+\frac{1}{2}} &= \begin{cases} m_{i,j}, & \text{if } \Psi_{i,j} \geq \Psi_{i,j+1} \\ m_{i,j+1}, & \text{if } \Psi_{i,j+1} > \Psi_{i,j} \end{cases} \\ m_{i+\frac{1}{2},j} &= \begin{cases} m_{i,j}, & \text{if } \Psi_{i,j} \geq \Psi_{i+1,j} \\ m_{i+1,j}, & \text{if } \Psi_{i+1,j} > \Psi_{i,j} \end{cases} \end{aligned} \quad (\text{E11})$$

With these definitions, the discretized Laplacian is

$$\begin{aligned} \nabla \cdot (m_t K \nabla \Psi_2^n) &= [m_{i,j+\frac{1}{2}} K_{i,j+\frac{1}{2}} (\Psi_{i,j+1} - \Psi_{i,j}) \\ &\quad - m_{i,j-\frac{1}{2}} K_{i,j-\frac{1}{2}} (\Psi_{i,j} - \Psi_{i,j-1}) \\ &\quad + m_{i+\frac{1}{2},j} K_{i+\frac{1}{2},j} (\Psi_{i+1,j} - \Psi_{i,j}) \\ &\quad - m_{i-1/2,j} K_{i-\frac{1}{2},j} (\Psi_{i,j} - \Psi_{i-1,j})] \frac{1}{\Delta h^2} \end{aligned} \quad (\text{E12})$$

We implement the no-flow condition Eq. (A9) by imposing the following conditions:

$$\begin{aligned} \Psi_{i,j+1} - \Psi_{i,j} &= 0, \text{ if } j = N_x, \\ \Psi_{i,j} - \Psi_{i,j-1} &= 0, \text{ if } j = 1, \\ \Psi_{i+1,j} - \Psi_{i,j} &= 0, \text{ if } i = N_z, \\ \Psi_{i,j} - \Psi_{i-1,j} &= 0, \text{ if } i = 1, \end{aligned} \quad (\text{E13})$$

Hence, we get large sparse linear systems from both the potential equation or the saturation equation, and we use an Algebraic Multi-grid Method (AMG) solver (AMGCL) (Demidov, 2017) to solve them.

## E2 Backward

Since  $f_{\text{op1}}$  and  $f_{\text{op2}}$  can be implemented with built-in operators in the AD framework, the backward operators  $b_{\text{op1}}$  and  $b_{\text{op2}}$  are automatically handled. The remaining two operators  $f_{\text{op3}}$  and  $f_{\text{op4}}$  are customized operators, so we need to implement the backward operators  $b_{\text{op3}}$  and  $b_{\text{op4}}$ <sup>1</sup>:

$$\frac{\partial \mathcal{J}}{\partial \Psi_2^n} \frac{\partial f_{\text{op3}}}{\partial K}, \frac{\partial \mathcal{J}}{\partial \Psi_2^n} \frac{\partial f_{\text{op3}}}{\partial m_t}, \frac{\partial \mathcal{J}}{\partial \Psi_2^n} \frac{\partial f_{\text{op3}}}{\partial \bar{q}^n} = b_{\text{op3}} \left( \frac{\partial \mathcal{J}}{\partial \Psi_2^n}, \Psi_2^n, K, m_t, \bar{q}^n \right) \quad (\text{E14})$$

$$\begin{aligned} & \frac{\partial \mathcal{J}}{\partial S_2^{n+1}} \frac{\partial f_{\text{op4}}}{\partial S_2^n}, \frac{\partial \mathcal{J}}{\partial S_2^{n+1}} \frac{\partial f_{\text{op4}}}{\partial K}, \frac{\partial \mathcal{J}}{\partial S_2^{n+1}} \frac{\partial f_{\text{op4}}}{\partial \Psi_2^n} \\ & = b_{\text{op4}} \left( \frac{\partial \mathcal{J}}{\partial S_2^{n+1}}, S_2^{n+1}, S_2^n, K, \Psi_2^n, \phi, q_2^n \right) \end{aligned} \quad (\text{E15})$$

We demonstrate how to implement  $\frac{\partial \mathcal{J}}{\partial S_2^{n+1}} \frac{\partial f_4}{\partial K}$  as example. The rest backward operators are implemented similarly. First, the PDE-constraint can be written as

$$\begin{aligned} & \mathcal{H}(S_2^{n+1}, S_2^n, \Psi_2^n, K) \\ & = \phi(S_2^{n+1} - S_2^n) - \nabla \cdot (m_2(S_2^{n+1})K \nabla \Psi_2^n) \Delta t - \left( q_2^n + q_1^n \frac{m_2(S_2^{n+1})}{m_1(S_2^{n+1})} \right) \Delta t = 0 \end{aligned} \quad (\text{E16})$$

The discretization in both space and time is.

$$\begin{aligned} & \phi_{i,j} (S_{2;i,j}^{n+1} - S_{2;i,j}^n) - [m_{2;i,j+\frac{1}{2}} K_{i,j+\frac{1}{2}} (\Psi_{2;i,j+1} - \Psi_{2;i,j}) - m_{2;i,j-\frac{1}{2}} K_{i,j-\frac{1}{2}} (\Psi_{2;i,j} - \Psi_{2;i,j-1}) \\ & + m_{2;i+\frac{1}{2},j} K_{i+\frac{1}{2},j} (\Psi_{2;i+1,j} - \Psi_{2;i,j}) - m_{2;i-1/2,j} K_{i-1/2,j} (\Psi_{2;i,j} - \Psi_{2;i-1,j})] \frac{\Delta t}{\Delta h^2} \\ & - \left( q_{2;i,j}^n + q_{1;i,j}^n \frac{m_{2;i,j}}{m_{1;i,j}} \right) \frac{\Delta t}{h^2 h_y} = 0. \end{aligned} \quad (\text{E17})$$

The symbol  $S_{2;i,j}^{n+1}$ , for example, stands for saturation  $S_2$  at time step  $n$  and at the center of cell  $i, j$ . The mobilities at half grid points are computed with Eq. (E11), where  $m_{1;i,j}$  and  $m_{2;i,j}$  are functions of the unknown saturation  $S_{2;i,j}^{n+1}$ . At the boundaries, we insert the discrete boundary conditions (Eq. (E13)) in Eq. (E17).

According to the recipe in Section 3 on deriving backward operators in AD for implicit time-schemes:

1. We first follow Eq. (28) to construct a linear system

$$\mathcal{H}_{S_2^{n+1}}^T \boldsymbol{\lambda} = - \left( \frac{\partial \mathcal{J}}{\partial S_2^{n+1}} \right)^T, \quad (\text{E18})$$

and solve for the Lagrange multiplier  $\boldsymbol{\lambda}$ . The left-hand side of the equation is also the transpose of the Jacobian matrix used in the Newton-Raphson method. We assemble the Jacobian matrix by taking the derivative of  $\mathcal{H} = 0$  with respect to  $S_2^{n+1}$  in Eq. (E17) (including the mobilities) for every  $(i, j)$ , and put each of the row vectors in the matrix according to the row-major sequence in  $(i, j)$ .

2. Assemble the Jacobian matrix of parameters. For example, to compute  $\frac{\partial \mathcal{J}}{\partial S_2^{n+1}} \frac{\partial f_{\text{op4}}}{\partial K}$ , we take the derivative of  $\mathcal{H} = 0$  with respect to  $K$  and assemble the matrix  $\mathcal{H}_K$  in the same manner as in step 1.
3. Compute backward outputs. For example,

$$\frac{\partial \mathcal{J}}{\partial S_2^{n+1}} \frac{\partial f_{\text{op1}}}{\partial K} = \boldsymbol{\lambda}^T \mathcal{H}_K. \quad (\text{E19})$$

<sup>1</sup> In this project, we write these parts in C++ according to the interface of TensorFlow, but the AD-CME package can also take care of code written in other languages.

## Appendix F The Newton-Raphson Method

We briefly outline the Newton-Raphson method to compute  $S_2^{n+1}$  from  $S_2^n$  for the nonlinear saturation equation. First, we define the residual vector as

$$R(S) = \phi(S - S_2^n) - \nabla \cdot (m_2(S)K\nabla\Psi_2^n) \Delta t - q_2^n \Delta t. \quad (\text{F1})$$

Using Taylor expansion, we have

$$R(S) = R(S_2^n) + R'(S_2^n)(S - S_2^n) + \mathcal{O}(\|S - S_2^n\|). \quad (\text{F2})$$

Since the residual function equals zero vector at  $S_2^{n+1}$ , we attempt to find  $S$  that satisfy this condition, and then arrive at

$$-R(S_2^n) = R'(S_2^n)\Delta S, \quad (\text{F3})$$

where  $R'(S_2^n)$  is the Jacobian matrix of  $R$  with respect to  $S_2$  at  $S_2^n$ . Solving sparse system, we obtain  $\Delta S$  and make the update

$$S \leftarrow S + \alpha\Delta S, \quad (\text{F4})$$

where  $\alpha$  is the step length that is set as 1 initially. If the updated  $S$  does not reduce the norm of the residual function, or it is not within the bounds of  $[0, 1]$ , we divide  $\alpha$  by half ( $\alpha = 0.5 \alpha$ ) and update  $S$  with the new  $\alpha$  until those requirements are satisfied. This is the back-tracking line search for one Newton iteration. Then, we repeat the process until the convergence criterion is met: relative changes in the norm of the residual vectors are small than a given threshold. Hence, we find the saturation at time step  $n + 1$ .

## Acknowledgments

The authors thank Biondo Biondi, Tapan Mukerji, and Gerald Mavko for many helpful discussions.

## References

- Abadi, M., Barham, P., Chen, J., Chen, Z., Davis, A., Dean, J., ... others (2016). Tensorflow: A system for large-scale machine learning. In (pp. 265–283).
- Anderson, J. E., Tan, L., & Wang, D. (2012). Time-reversal checkpointing methods for rtm and fwi. *Geophysics*, *77*(4), S93–S103.
- Aster, R. C., Borchers, B., & Thurber, C. H. (2013). Chapter four - tikhonov regularization. In R. C. Aster, B. Borchers, & C. H. Thurber (Eds.), *Parameter estimation and inverse problems (second edition)* (Second Edition ed., p. 93 - 127). Boston: Academic Press. Retrieved from <http://www.sciencedirect.com/science/article/pii/B9780123850485000045>  
doi: <http://dx.doi.org/10.1016/B978-0-12-385048-5.00004-5>
- Aziz, K. (1979). Petroleum reservoir simulation. *Applied Science Publishers*, *476*.
- Beaujean, J., Nguyen, F., Kemna, A., Antonsson, A., & Engesgaard, P. (2014). Calibration of seawater intrusion models: Inverse parameter estimation using surface electrical resistivity tomography and borehole data. *Water Resources Research*, *50*(8), 6828–6849.
- Brie, A., Pampuri, F., Marsala, A., Meazza, O., et al. (1995). Shear sonic interpretation in gas-bearing sands. In *Spe annual technical conference and exhibition*.
- Byrd, R. H., Lu, P., Nocedal, J., & Zhu, C. (1995). A limited memory algorithm for bound constrained optimization. *SIAM Journal on Scientific Computing*, *16*(5), 1190–1208.
- Crichlow, H. B. (1977). *Modern reservoir engineering: a simulation approach*. Prentice hall.

- Daley, T. M., Ajo-Franklin, J. B., & Doughty, C. (2011). Constraining the reservoir model of an injected co2 plume with crosswell csm at the frio-ii brine pilot. *International Journal of Greenhouse Gas Control*, 5(4), 1022–1030.
- Demidov, D. (2017). Amgcl: An efficient, flexible, and extensible algebraic multigrid. *Lobachevskii Journal of Mathematics*, 40, 535–546.
- Emerick, A. A., Moraes, R., Rodrigues, J., et al. (2007). History matching 4d seismic data with efficient gradient based methods. In *Europec/eage conference and exhibition*.
- Evans, M. W., Harlow, F. H., & Bromberg, E. (1957). *The particle-in-cell method for hydrodynamic calculations* (Tech. Rep.). LOS ALAMOS NATIONAL LAB NM.
- Fohring, J., Haber, E., & Ruthotto, L. (2014). Geophysical imaging of fluid flow in porous media. *SIAM Journal on Scientific Computing*, 36(5), S218–S236.
- Huang, X., Meister, L., & Workman, R. (1998). Improving production history matching using time-lapse seismic data. *The Leading Edge*, 17(10), 1430–1433.
- Landa, J. L., Horne, R. N., et al. (1997). A procedure to integrate well test data, reservoir performance history and 4-d seismic information into a reservoir description. In *Spe annual technical conference and exhibition*.
- Li, D., & Harris, J. M. (2018). Full waveform inversion with nonlocal similarity and model-derivative domain adaptive sparsity-promoting regularization. *Geophysical Journal International*, 215(3), 1841–1864.
- Li, R., Reynolds, A. C., Oliver, D. S., et al. (2001). History matching of three-phase flow production data. In *Spe reservoir simulation symposium*.
- Lie, K.-A. (2019). *An introduction to reservoir simulation using matlab/gnu octave*. Cambridge University Press.
- Marotzke, J., Giering, R., Zhang, K. Q., Stammer, D., Hill, C., & Lee, T. (1999). Construction of the adjoint mit ocean general circulation model and application to atlantic heat transport sensitivity. *Journal of Geophysical Research: Oceans*, 104(C12), 29529–29547.
- Martin, R., Komatitsch, D., & Ezziani, A. (2008). An unsplit convolutional perfectly matched layer improved at grazing incidence for seismic wave propagation in poroelastic media. *Geophysics*, 73(4), T51–T61.
- Mavko, G., Mukerji, T., & Dvorkin, J. (2009). *The rock physics handbook: Tools for seismic analysis of porous media*. Cambridge university press.
- McLaughlin, D., & Townley, L. R. (1996). A reassessment of the groundwater inverse problem. *Water Resources Research*, 32(5), 1131–1161.
- Oliver, D. S., & Chen, Y. (2011). Recent progress on reservoir history matching: a review. *Computational Geosciences*, 15(1), 185–221.
- Reid, L. B. (1996). *A functional inverse approach for three-dimensional characterization of subsurface contamination* (Unpublished doctoral dissertation). Massachusetts Institute of Technology.
- Shi, J.-Q., Imrie, C., Sinayuc, C., Durucan, S., Korre, A., & Eiken, O. (2013). Snøhvit co2 storage project: Assessment of co2 injection performance through history matching of the injection well pressure over a 32-months period. *Energy Procedia*, 37, 3267–3274.
- Tarantola, A. (1984). Inversion of seismic reflection data in the acoustic approximation. *Geophysics*, 49(8), 1259–1266.
- Teletzke, G. F., Wattenbarger, R. C., Wilkinson, J. R., et al. (2010). Enhanced oil recovery pilot testing best practices. *SPE Reservoir Evaluation & Engineering*, 13(01), 143–154.
- Virieux, J., & Operto, S. (2009). An overview of full-waveform inversion in exploration geophysics. *Geophysics*, 74(6), WCC1–WCC26.
- Volkov, O., Bukshynov, V., Durlafsky, L. J., & Aziz, K. (2018). Gradient-based pareto optimal history matching for noisy data of multiple types. *Computa-*



*tional Geosciences*, 22(6), 1465–1485.

- Wang, K.-Y., Lary, D., Shallcross, D., Hall, S., & Pyle, J. (2001). A review on the use of the adjoint method in four-dimensional atmospheric-chemistry data assimilation. *Quarterly Journal of the Royal Meteorological Society*, 127(576), 2181–2204.
- Zhang, Q., Mao, W., Zhou, H., Zhang, H., & Chen, Y. (2018). Hybrid-domain simultaneous-source full waveform inversion without crosstalk noise. *Geophysical Journal International*, 215(3), 1659–1681.